The S1 helix critically regulates the finely tuned gating of Kv11.1 channels

Received for publication, January 31, 2017, and in revised form, February 26, 2017 Published, Papers in Press, March 9, 2017, DOI 10.1074/jbc.M117.779298

Kevin Phan[‡§1], Chai Ann Ng[‡§1], Erikka David[‡], Dmitry Shishmarev[¶], Philip W. Kuchel[¶], Jamie I. Vandenberg[‡§], and Matthew D. Perry[‡§2]

From the [‡]Victor Chang Cardiac Research Institute, 405 Liverpool Street, Darlinghurst, New South Wales 2010, the [§]St. Vincent's Clinical School, University of New South Wales, New South Wales 2052, and the [¶]School of Life and Environmental Sciences, The University of Sydney, Sydney, New South Wales 2006, Australia

Edited by F. Anne Stephenson

Congenital mutations in the cardiac Kv11.1 channel can cause long QT syndrome type 2 (LQTS2), a heart rhythm disorder associated with sudden cardiac death. Mutations act either by reducing protein expression at the membrane and/or by perturbing the intricate gating properties of Kv11.1 channels. A number of clinical LQTS2-associated mutations have been reported in the first transmembrane segment (S1) of Kv11.1 channels, but the role of this region of the channel is largely unexplored. In part, this is due to problems defining the extent of the S1 helix, as a consequence of its low sequence homology with other Kv family members. Here, we used NMR spectroscopy and electrophysiological characterization to show that the S1 of Kv11.1 channels extends seven helical turns, from Pro-405 to Phe-431, and is flanked by unstructured loops. Functional analysis suggests that pre-S1 loop residues His-402 and Tyr-403 play an important role in regulating the kinetics and voltage dependence of channel activation and deactivation. Multiple residues within the S1 helix also play an important role in fine-tuning the voltage dependence of activation, regulating slow deactivation, and modulating C-type inactivation of Kv11.1 channels. Analyses of LQTS2-associated mutations in the pre-S1 loop or S1 helix of Kv11.1 channels demonstrate perturbations to both protein expression and most gating transitions. Thus, S1 region mutations would reduce both the action potential repolarizing current passed by Kv11.1 channels in cardiac myocytes, as well as the current passed in response to premature depolarizations that normally helps protect against the formation of ectopic beats.

Kv11.1 channels, otherwise known as human *ether-a-go-go*-related gene (hERG)[3] potassium channels, play a crucial role in repolarization of the cardiac action potential (1) and in the suppression of arrhythmias caused by premature stimuli (2, 3). Inherited mutations in *KCNH2*, the gene that encodes Kv11.1 channels, can result in long QT syndrome type 2 (LQTS2), an electrical disorder of the heart that dramatically increases the risk of cardiac arrhythmias and sudden cardiac death (4–8). At present, over 500 *KCNH2* variants have been identified (9). LQTS2 mutations can be classified according to their mechanism of action, namely (i) altered protein biogenesis (10), (ii) impaired protein expression at the membrane (11–14), (iii) defective channel gating or ion permeation (15), or (iv) combined perturbations to expression and function (16–19).

Kv11.1 channels function as tetramers, with each subunit composed of six helical transmembrane segments, S1–S6 (8). The first four segments (S1–S4) make up the voltage sensor domain (VSD), whereas the S5 and S6 helices, as well as the intervening pore helix (PH) and selectivity filter, constitute the pore domain (8). Pore domains from each subunit surround the central conduction pathway, creating two gates that control the flow of ions as follows: an activation gate, formed by the cytoplasmic ends of the four S6 helices, and a C-type inactivation gate located at the selectivity filter (8). Thus, Kv11.1 channels can exist in the following three main conformations: closed, open, or inactivated. Activation (closed-to-open) of Kv11.1 channels is much slower than for other voltage-gated K^+ channels (Kv) (3, 8). Channel deactivation (open-to-closed) also exhibits slow kinetics, partly mediated by cytoplasmic N- and C-terminal interactions of the protein (20–23). In contrast, the C-type inactivation is rapid and intrinsically voltage-dependent (24). These unique features of the Kv11.1 channels make them ideally suited to their role as regulators of heart rhythm.

In Kv channels, it is well established that membrane depolarization drives movement of the positively charged S4 helix within the membrane bilayer, toward the extracellular interface (8). This motion releases mechanical force on the S4-S5 linker, which in turn allows the S6 activation gate to open (25, 26). It is unclear whether deactivation follows the same transition pathway in reverse or whether it involves a different set of intermediate states (27). Although the role of the S4 helix has been

This work was supported in whole or part by Australian Research Council Discovery Grant DP150101929, National Health and Medical Research Council Program Grant App1074386, and National Health and Medical Research Council Fellowship App1116948 (to J. I. V). The authors declare that they have no conflicts of interest with the contents of this article.
This article was selected as one of our Editors' Picks.
This article contains supplemental Tables S1–S3.

[1] Both authors should be considered joint first authors.
[2] To whom correspondence should be addressed: Mark Cowley Lidwill Research Programme in Cardiac Electrophysiology, the Victor Chang Cardiac Research Institute, 405 Liverpool St., Darlinghurst, New South Wales 2010, Australia, Tel.: 61-2-9295-8687; Fax: 61-2-9295-8601; E-mail: m.perry@victorchang.edu.au.

[3] The abbreviations used are: hERG, human ether-a-go-go related gene; S1, transmembrane segment 1; LQTS2, long QT syndrome type 2; $I_{Kv11.1}$, current recorded from Kv11.1 channels; cNBHD, cyclic nucleotide-binding homology domain; Kv, voltage-gated potassium channel; PH, pore helix; VSD, voltage sensor domain; EAG1, *ether-a-go-go* 1; FG, fully glycosylated; CG, core-glycosylated; CSI, chemical shift index; ANOVA, analysis of variance.

extensively characterized, other segments of the VSD are less well studied. For example, the S1 helix has been thought to be relatively immobile, acting only as a stabilizing anchor by forming charge pair interactions with the S4 helix (28–31). Recent studies on other Kv channels have suggested that the S1 helix forms important interactions with the S2 and/or S4 helices, which may help the S1 helix steer S4 motion during activation gating (32, 33). The S1 helix may also form important interactions with the S5 helix to anchor the VSD and pore domains of adjacent subunits (34–36), which is important for both gating and protein maturation of Kv2.1 channels (34). In Kv11.1 channels, more than 38 clinical LQTS2 mutations have been observed within the VSD (data from the International Long QT Registry), of which over one-third lie within the vicinity of the putative S1 helix, further indicating that this region may be important for channel expression and/or function.

A short intracellular helical segment located just prior to the transmembrane S1 helix has been observed in recent protein structures of a range of Kv channels, such as the Kv1.2/2.1 chimera (37), Slo2.2 (38), and $K_{Ca}1.1$ (also termed BK (39, 40)), as well as various TRP channels, including TRPV channels (41–43) and TRPA1 channels (44). Termed the pre-S1, S0, or S0′ helix, this short helical segment may play a role in the biogenesis, protein-folding, and inter-subunit interactions of TRPV channels (45). In TRPA1 channels, the pre-S1 contains several cysteine and lysine residues that are involved in channel activation by electrophilic agonists (44). The existence of a "pre-S1" helix in Kv11.1 channels, and its potential role in channel expression or function, has not been examined.

A major challenge to understanding the role of the S1 region in Kv11.1 channels is that this region exhibits poor sequence homology to other members of the Kv channel superfamily. Pairwise and global sequence alignments demonstrate sequence identities ranging between 5.9 and 19% and sequence similarities ranging between 28 and 44% for the region surrounding the putative S1 helix (28, 35, 46–49). Such low sequence homology has made an analysis of the extent of the S1 helix problematic. Several previous studies have reported putative S1 helices in Kv11.1 channels, but the starting amino acid varies from Ser-404 (ending Phe-424) to Val-409 (ending Leu-433) (28, 35, 46–49), almost two helical turns different. Recently, Whicher and MacKinnon (50) published a structure of the rat ether-a-go-go 1 (EAG1) channel. EAG1 (also termed Kv10.1) and Kv11.1 are members of the same family of Kv channels and share a high degree of homology even within the putative S1 region. This has enabled us to narrow down the putative S1 region and to examine the contribution of this segment in fine-tuning the gating kinetics of Kv11.1 channels. Accordingly, the aims of this study were as follows: 1) to use NMR spectroscopy to estimate the transmembrane limits of the S1 helix; 2) to investigate to what extent mutations of the S1 segment affect the gating properties of Kv11.1 channels; and 3) to examine how LQTS2-associated mutations in the pre-S1 and S1 regions alter the expression and function of Kv11.1 channels.

Results

Structural extent of the S1 helix of Kv11.1 channels

To examine the structural extent of the S1 helix in Kv11.1 channels, we used NMR spectroscopy to analyze a 45-residue synthetic peptide spanning from Arg-394 to Glu-438, a region extending well beyond the N- and C-terminal limits of the S1 predictions from the published literature (28, 35, 46–49). To mimic the membrane environment, we studied the synthetic S1 peptide in SDS micelles (see Fig. 1*A*). As the peptide contains several amino acids of the same type (*i.e.* 7 leucines, 4 isoleucines, 4 alanines, and 3 valines), there was considerable overlap of signals in the aliphatic region of the NMR spectrum (see Fig. 1*A*). Proton (^{1}H) resonances of Cα were assigned for 42/45 residues, with the exceptions being His-402, Ile-414, and Ile-419. Nevertheless, the stretch of negative chemical shift index (CSI) values of the ^{1}H resonance of Cα suggested that at least two regions, from Trp-410 to Phe-424 and from Tyr-427 to Leu-432, adopted helical conformations (see Fig. 1*B*). The positive CSI values for Thr-425 and Pro-426 suggest that there may be a break or "kink" between the two helical segments. For the residues prior to Trp-410, or after Leu-432, there are no consecutive residues with negative CSI values, suggesting that these regions are not helical in the peptide.

To investigate whether the helical region from Trp-410 to Leu-432 was likely to represent the transmembrane helix of S1, we repeated the NMR experiments in the presence of Gd^{3+}, a paramagnetic agent that suppresses signals from residues located within the micelle environment (51). Data for each residue is presented as the fraction of ^{1}H signal remaining after addition of Gd^{3+}. A value close to 1 indicates no suppression of the ^{1}H signal by Gd^{3+} and suggests that the corresponding residue is likely to be located within the micelle environment (*i.e.* within the transmembrane region), whereas a value of 0 indicates complete suppression by Gd^{3+}, suggesting that the corresponding residue lies outside of the micelle environment (*i.e.* outside of the transmembrane region). Gd^{3+} suppressed signals in the region Arg-394 to Ala-408, whereas the signals for residues Trp-410 to Glu-435 were largely unaltered (Fig. 1*C*). The NMR data suggest that the transmembrane extent of S1 in Kv11.1 extends at least from Trp-410 to Leu-432, with a possible break or kink at Thr-425/Pro-426. The NMR data do not support a pre-S1 helical segment in Kv11.1 channels, a feature that is present in the structure of other voltage-gated ion channels (37–43) but not in the cryo-electron microscopy (cryo-EM) structure of rEAG (50).

Next, we generated a homology model based on the structure of rEAG (50), a related channel protein family member with high sequence similarity to Kv11.1. In the homology model shown in Fig. 2, the S1 helix (shown in *white* in Fig. 2*B*) begins at Pro-405 and extends over seven helical turns to Phe-431, with no apparent breaks in the helical structure. However, there appears to be a notable kink in the S1 helix around residues Phe-424–Thr-425–Pro-426 (see Fig. 2). Structural analysis of the model predicts that residues within the S1 helix form a plethora of interactions with residues in the S2 (Fig. 2*B*, *cyan*), S3 (*light green*), S4 (*orange*), and S5 (*blue*) helices, as well as the pore helix (*dark green*). The pre-S1 region is a flexible intracel-

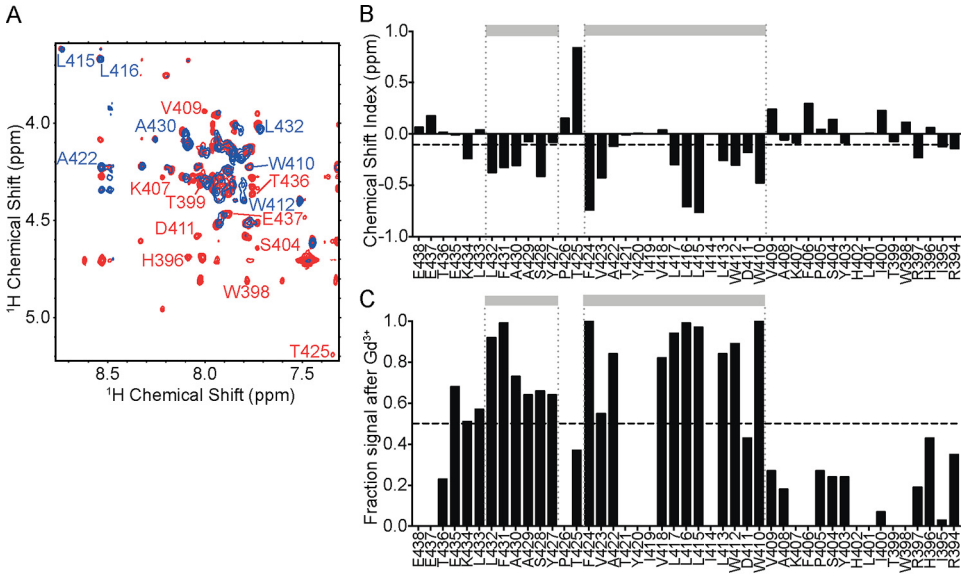

Figure 1. Structural analysis of a peptide corresponding to the extended S1 region of Kv11.1 channels, using NMR spectroscopy. *A,* NOESY spectrum showing the amide-Hα cross-peaks in the absence (*red*) and presence (*blue*) of Gd^{3+}. Note the considerable spectral overlap in the central region (4.1–4.4 ppm on the *y* axis and 7.8–8.1 ppm on the *x* axis). Examples of peaks that are clearly visible in both the presence and absence of Gd^{3+} are labeled in *blue*, and examples of peaks that are suppressed by Gd^{3+} are labeled in *red*. The suppressed peaks mostly correspond to residues at the N and C termini, whereas non-suppressed peaks correspond to residues in the central region of the peptide. *B,* plot of the CSI for Cα ^{1}H resonances of the S1 peptide in SDS micelles. Stretches of resonances with CSI values < -0.1, which are not interrupted by residues with a chemical shift index of >0.1, are indicative of α-helical secondary structure (*i.e.* Trp-410 to Phe-424). *C,* fractional of ^{1}H resonance peak intensity remaining after the addition of Gd^{3+}. Gd^{3+} acts as a paramagnetic relaxation reagent that suppresses the ^{1}H signals from residues located outside of the micelle environment. Most of the residues between Trp-410 to Glu-435 are protected (>50%) from suppression by Gd^{3+} (indicated by values closer to 1), indicating that this region lies within the detergent micelle and thus likely represents the transmembrane helix of S1.

lular loop beginning at Asp-383 and extending to Ser-404. The region immediately after S1, starting at Leu-432, is a flexible extracellular loop up to Glu-437, after which it transitions into the S2 helix.

Functional role(s) of the S1 helix in Kv11.1 channels

To investigate the functional role(s) of the putative pre-S1 loop (Arg-394 to Ser-404), S1 helix (Pro-405 to Phe-431), and post-S1 loop (Leu-432 to Glu-435) in Kv11.1 channels, we compared the gating properties of mutant channels, in which each residue was individually mutated to alanine (or from alanine to valine), with wild type (WT). Similar approaches that use perturbations from scanning mutagenesis to assess the role and interaction partners for various helices and regions of the voltage sensor domain have been applied to other voltage-gated potassium channels (52–55), as well as to other helices of the voltage sensor domain in Kv11.1 channels (56). In this study perturbations to the equilibrium of activation or inactivation gating parameters are reported as changes in the Gibbs free energy ($\Delta\Delta G$) of the transition, compared with WT, whereas perturbations to the rates of activation, deactivation, onset of inactivation, or recovery from inactivation are reported as changes in ln*k* relative to WT ($-\Delta\ln k$). Perturbations were considered relevant if they met two criteria as follows: first, that the ΔG or ln*k* value was significantly different to WT (using ANOVA, $p < 0.05$), and second, if the $-\Delta\ln k$ value was $> \pm 0.693\ s^{-1}$, which is equivalent to a doubling of the rate, or the $\Delta\Delta G$ value was $> \pm 0.5$ kcal·mol^{-1}, which has previously been shown to be a biologically relevant cutoff for shifts in equilibria (57, 58).

First, we investigated whether individual mutations altered the voltage dependence of channel activation, as this is one of the principal functions of the voltage-sensing domain in Kv channels. Using the voltage protocol shown in the *upper panel* of Fig. 3*A*, we measured the voltage at which half the maximum number of channels are open ($V_{0.5}$) after a 1-s pre-pulse. Exemplar families of currents recorded from oocytes expressing WT or mutant channels are shown in Fig. 3*A*. In the flexible pre-S1 loop, there was a small group of three mutations (L401A, H402A, and Y403A) that caused significant hyperpolarizing shifts in the voltage dependence of channel activation (see supplemental Table 1). As shown by the current trace (Fig. 3*A*) and current-voltage plot (Fig. 3*B*) for Y403A, this mutation caused the largest shift in voltage dependence of activation ($V_{0.5}$) from -12.1 ± 0.9 mV in WT ($n = 7$) to -36.8 ± 1.4 mV in Y403A ($n = 7$). Y403A also exhibited a steeper slope in the voltage dependence of activation (5.7 ± 0.2 mV *versus* 8.8 ± 0.2 mV for WT). Combined, the perturbations to the $V_{0.5}$ and slope correspond to a change in Gibbs free energy of activation ($\Delta\Delta G_{act}$) of -3.0 ± 0.2 kcal mol^{-1} for Y403A ($p < 0.05$ using ANOVA, Fig. 3*C*). Significant hyperpolarizing shifts in the voltage dependence of activation were observed for 11 mutations in the putative S1 helix (see Fig. 3*C*). Notably, D411A shifted the $V_{0.5}$ to -42.7 ± 0.8 mV and the slope to 7.1 ± 0.2 mV ($n = 8$, Fig. 3, *A* and *B*), corresponding to a $\Delta\Delta G_{Act}$ of -2.7 ± 0.2 kcal mol^{-1} ($p < 0.05$ using ANOVA, Fig. 3*C*). In comparison, only three mutations in the S1 helix induced significant depolarizing shifts in the voltage dependence of activation (Fig. 3*C*). The largest depolarizing shift was observed for the T421A mutation, which exhibited a $V_{0.5}$ of $+16.1 \pm 0.7$ mV and a shallower slope of

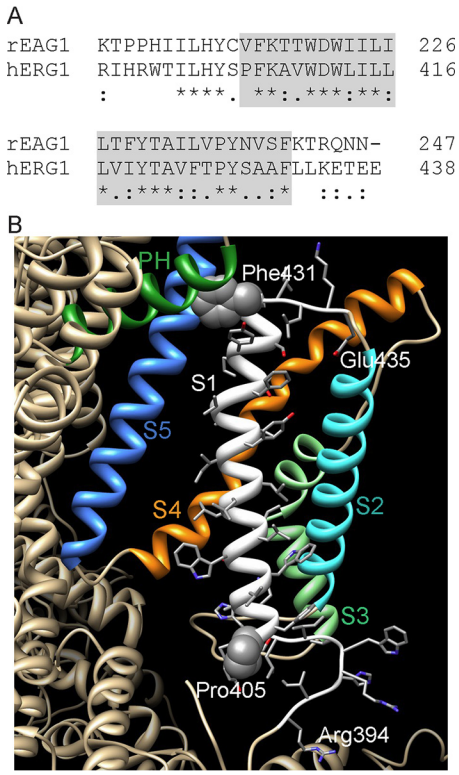

Figure 2. Extent of the S1 transmembrane segment in Kv11.1 channels. *A,* amino acid sequence alignment of the extended S1 region (corresponding to the Kv11.1 S1 peptide shown in Fig. 1) of rEAG and Kv11.1 (hERG1) channels. * denotes fully conserved amino acids, and colon and period denote amino acids with strongly or weakly conserved properties, respectively. The *gray box* indicates the extent of the S1 helix based on the cryo-EM structure of rEAG channels (50). *B,* homology model of a Kv11.1 channel based on the cryo-EM structure of the rEAG channel (50). The S1 helix (shown in *white*) extends from Pro-405 to Phe-431 (side chains shown in *space fill*), with no apparent breaks in the helical structure. Regions of the S1 helix lie close to other transmembrane helices from the same subunit, namely S2 (*cyan*), S3 (*light green*), S4 (*orange*), S5 (*blue*), and the pore helix (PH, *dark green*).

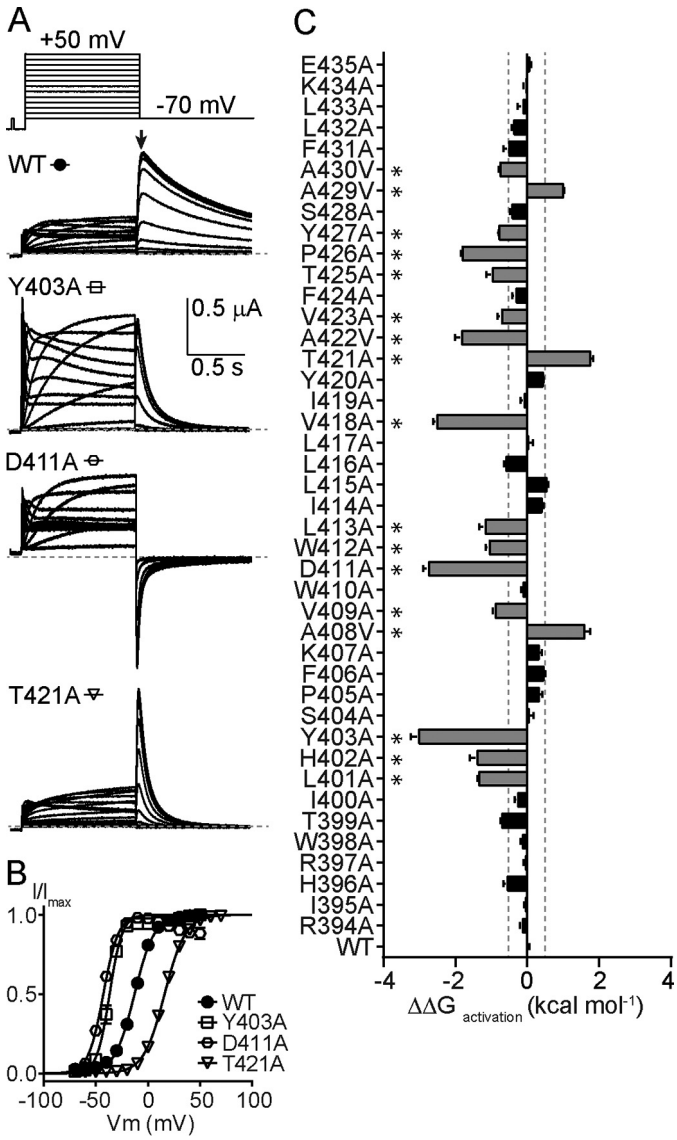

Figure 3. Mutagenesis of S1 residues perturbs the voltage dependence of Kv11.1 channel activation. *A,* typical families of currents recorded from WT, Y403A, D411A, or T421A Kv11.1 channels, in response to the voltage protocol shown in *upper panel* (and described under "Experimental procedures"). *Arrow* on *WT trace* indicates the peak tail current that is used to measure the maximal channel opening after each voltage pre-pulse. Note that tail currents for D411A are inward because they were measured at −120 mV, rather than −70 mV, due to the hyperpolarizing shift in the voltage dependence of activation observed with the D411A mutation. *B,* plot of mean (±S.E.) peak tail currents, normalized to the maximum, at each voltage for WT (*closed circles*), Y403A (*open squares*), D411A (*open diamonds*), and T421A (*open inverted triangles*). Data were fitted with a Boltzmann function to obtain the half-maximal voltage ($V_{0.5}$) and slope of activation (given in supplemental Table 1). *C,* summary plot of the change in the energetics of the voltage-dependent distribution between the closed and open states for each S1 alanine mutant. For WT and mutant channels, the $\Delta G_{activation}$ was calculated for each replicate ($n = 4$ to 15, see supplemental Table 1) by fitting the current-voltage plot with a modified version of the Boltzmann function (see "Experimental procedures"). The $\Delta G_{activation}$ for each replicate was then compared with the mean WT $\Delta G_{activation}$ to obtain $\Delta\Delta G_{activation}$ (*i.e.* $\Delta\Delta G = \Delta G_{Mt} - \Delta G_{WT}{}^{mean}$). Data are shown as mean ± S.E. *Gray bars* indicate mutants that produced $\Delta\Delta G_{activation}$ shifts greater than ± 0.5 kcal mol^{-1} (±0.5 also indicated with *dotted lines*), whereas * denotes mutants where the $\Delta G_{activation}$ was calculated as significantly different from WT using one-way ANOVA ($p < 0.05$).

9.8 ± 0.5 mV (Fig. 3, *A* and *B*), corresponding to a $\Delta\Delta G_{act}$ of +1.8 ± 0.1 kcal mol^{-1} ($p < 0.05$ using ANOVA, Fig. 3*C*). In contrast to the pre-S1 loop and S1 helix, none of the mutations in the post-S1 loop caused significant perturbations to ΔG_{act} (see Fig. 3*C* and supplemental Table 1). These data suggest that the pre-S1 loop and the S1 helix play significant roles in regulating the voltage dependence of Kv11.1 channel activation.

To further understand the role of the S1 region in mediating transitions between the closed and open state of Kv11.1 channels, we examined the effect of mutations on the kinetics of activation, measured at +20 mV, using an envelope-of-tails protocol (see *upper panel* of Fig. 4*A*). For WT Kv11.1 channels, the closed-to-open transition is much slower than in other Kv channels (8), with a time constant for activation at +20 mV ($\tau_{act,\,+20\,mV}$) of 225 ± 22 ms ($n = 5$). Example traces of WT and selected mutants are shown in Fig. 4*A*. In the pre-S1 loop, the same three mutations (L401A, H402A, and Y403A), which shifted the voltage dependence of activation, also significantly accelerated the rate of activation, with the largest effect again observed for Y403A: $\tau_{act,\,+20\,mV}$ = 45.3 ± 4.6 ms (n = 6, see supplemental Table 1), equivalent to a shift in $-\Delta\ln k_{activation,\,+20\,mV}$ of −1.61 ± 0.11 s^{-1} (n = 6, Fig. 4*B*). Similarly, within the S1 helix, 12 of the 14 mutations that perturbed the voltage dependence of activation also significantly perturbed the kinetics of activation (Fig. 4*B*). The largest perturbation was caused by mutation A408V, which had a remark-

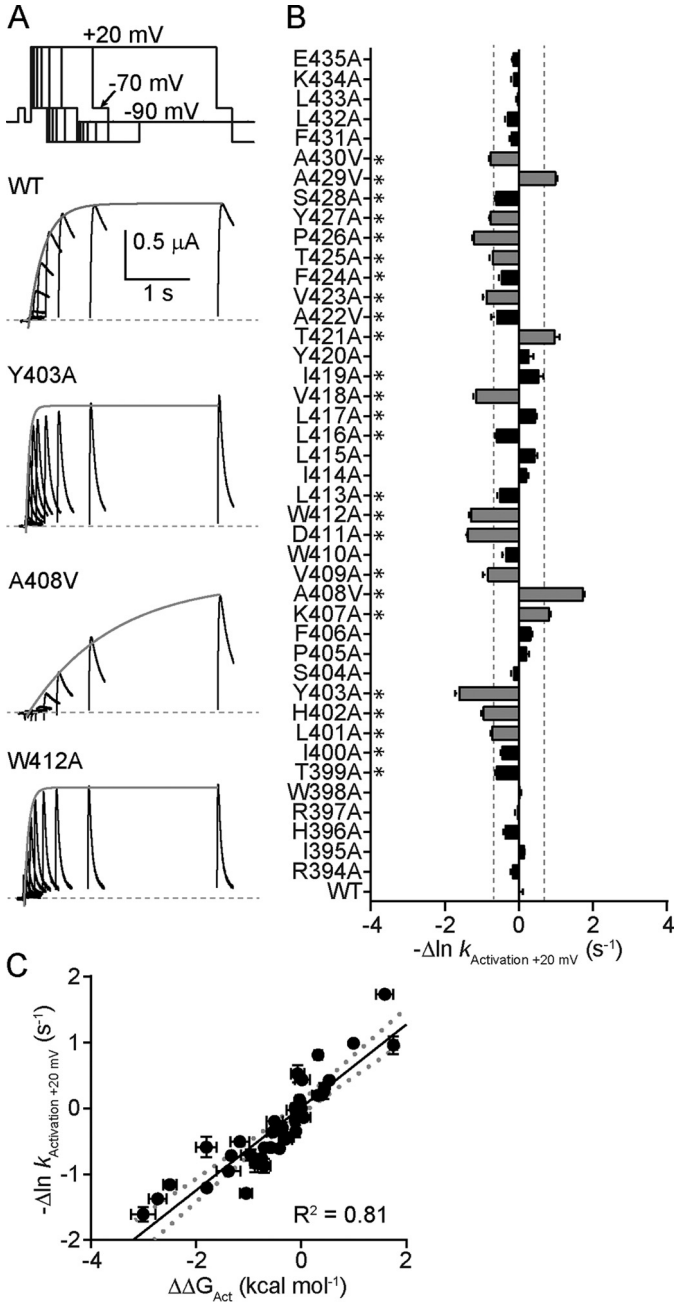

Figure 4. Altered kinetics of activation in response to mutation of S1 residues in Kv11.1 channels. *A,* typical families of currents recorded from WT, Y403A, A408V, or W412A Kv11.1 channels in response to the voltage protocol shown in *upper panel* (and described under "Experimental procedures"). Peak tail currents (measured at −70 mV) are plotted against the preceding activation pre-pulse time, and the family of peak tail currents is then fitted with a single exponential function (fits shown with *gray lines*) to obtain the time constant (τ) for activation at the pre-pulse voltage of +20 mV. *B,* summary plot of the change in the energetics of the rate of Kv11.1 channel activation for each S1 alanine mutant. For WT and mutant channels, the rate of activation at +20 mV ($\ln k_{\text{activation, +20 mV}}$) was calculated for each replicate (n = 3 to 15, see supplemental Table 1), see "Experimental procedures" for details. The $\ln k_{\text{activation, +20 mV}}$ for each replicate was then compared with the mean $\ln k_{\text{activation, +20 mV}}$ for WT, to obtain $-\Delta\ln k_{\text{activation, +20 mV}}$ (*i.e.* $\Delta\ln k_{\text{activation}} = \ln k_{\text{Mt}} - \ln k_{\text{WT}}{}^{\text{mean}}$). Data are shown as mean ± S.E. *Gray bars* indicate mutants that produced $-\Delta\ln k_{\text{activation, +20 mV}}$ shifts greater than ± 0.693 s^{-1} (± 0.693 also indicated with *dashed lines*), which is equivalent to a doubling of the rate. * denotes mutants where the $\ln k_{\text{activation, +20 mV}}$ was calculated as significantly different from WT using one-way ANOVA ($p <$ 0.05). *C,* correlation between the shift in the kinetics of activation ($-\Delta\ln k_{\text{activation, +20 mV}}$) and the shift in energetics of the voltage dependence of activation ($\Delta\Delta G_{\text{activation}}$) for each mutant. When fitted with a linear function, the R^2 value of 0.81 indicates that these processes are highly correlated.

ably slow $\tau_{\text{act, +20 mV}}$ of 1252.8 ± 44.6 ms (n = 8, see supplemental Table 1), a shift in $-\Delta\ln k_{\text{activation, +20 mV}}$ of +1.74 ± 0.04 s^{-1} (n = 6, Fig. 4*B*). Conversely, just one helical turn above Ala-408 in the S1 helix, mutations D411A or W412A caused pronounced accelerations in the rate of activation, with $\tau_{\text{act, +20 mV}}$ values of 56.0 ± 1.4 ms (n = 8) and 62.7 ± 4.0 ms (n = 15), corresponding to $-\Delta\ln k_{\text{activation, +20 mV}}$ shifts of −1.37 ± 0.03 and −1.29 ± 0.07 s^{-1}, respectively (see supplemental Table 1 and Fig. 4*B*). For almost all mutations, the shift in the voltage dependence of activation was sufficient to account for the majority of the perturbation observed in the rate of activation, as indicated from the robust linear fit (R^2 = 0.81) when these parameters were plotted against one another (Fig. 4*C*).

Next, we sought to determine whether mutations in the S1 region perturb the deactivation transition pathway, *i.e.* the conversion of channels from the open state to the closed state. To test this, we measured the rate of channel deactivation at voltages between −50 and −150 mV for WT and mutant Kv11.1 channels (see protocol in Fig. 5*A*). In WT Kv11.1 channels, the rate of deactivation is relatively slow compared with other Kv channels (20–23) and exhibits a voltage dependence such that deactivation is faster at more negative membrane voltages, *i.e.* faster at −120 mV (*black trace*) than at −70 mV (*gray trace*), as shown in Fig. 5*A*. Furthermore, when fitted with a double-exponential function, the relative proportion (λ) of the fast component is greater at −120 mV than at −70 mV (see supplemental Table 2). To enable comparison between mutants, we used an overall weighted time constant for deactivation ($\tau_{\text{deactivation, } X\text{ mV}}$), which is calculated by weighting τ_{fast} and τ_{slow} by their relative proportions, for calculations of $-\Delta\ln k_{\text{deactivation}}$ (see under "Experimental procedures"). Values for τ_{fast}, τ_{slow}, as well as the relative proportion of τ_{fast} ($\lambda_{\tau\text{fast}}$), are given in supplemental Table 2.

When examining perturbations to deactivation caused by S1 mutants, we observed quite different mutant profiles when measuring deactivation at −120 mV *versus* −70 mV. At −120 mV, only two mutants, Y403A in the pre-S1 loop and K407A in the S1 helix, significantly perturbed the rate of deactivation beyond the > ± 0.693 s^{-1} cutoff (Fig. 5*B, left panel*). In fact, the $-\Delta\ln k_{\text{deactivation, −120 mV}}$ of +3.14 ± 0.09 s^{-1} (n = 14) caused by K407A represents a dramatic slowing of deactivation, as demonstrated in Fig. 5*A*. In contrast, at a more physiological voltage of −70 mV, two mutants in the pre-S1 loop, 17 mutants in the S1 helix, and one mutant in the post-S1 loop significantly perturbed the rate of deactivation with values for $-\Delta\ln k_{\text{deactivation, −70 mV}} > \pm 0.693$ s^{-1} (Fig. 5*B, right panel*). In the pre-S1 loop, mutations H402A and Y403A significantly accelerated the rate of deactivation measured at −70 mV. Within the S1 helix, 12 mutants significantly accelerated the kinetics of deactivation, with the largest effect observed in the W412A mutation (Fig. 5, *A* and *B*). Five S1 mutants significantly slowed the rate of deactivation, whereas another two mutants, K407A and P426A, had deactivation rates at −70 mV that were

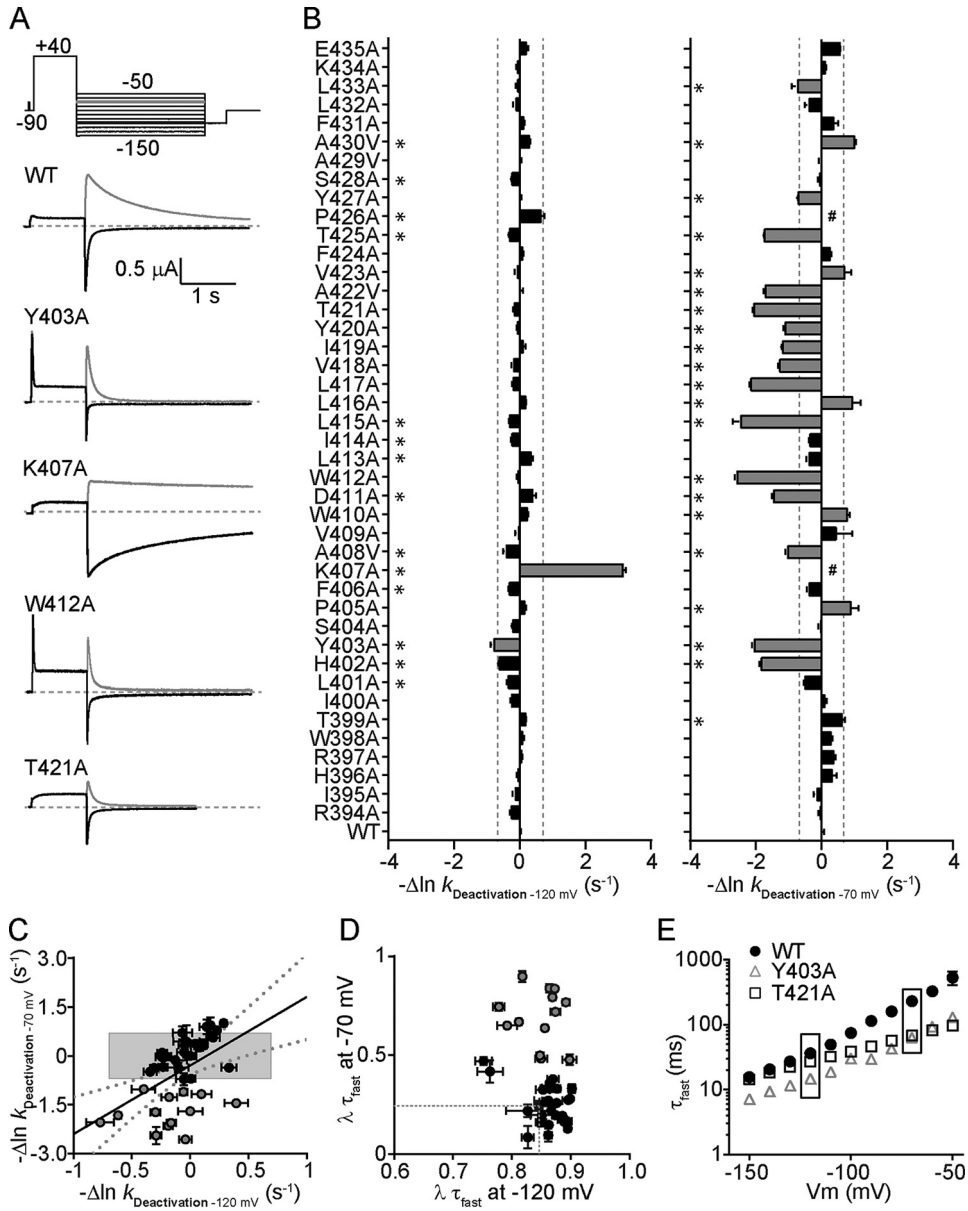

Figure 5. S1 helix residues play an important role in the slow kinetics of deactivation of Kv11.1 channels. *A,* typical families of currents recorded from WT, Y403A, K407A, W412A, or T421A Kv11.1 channels in response to the voltage protocol shown in *upper panel* (and described under "Experimental procedures"). For WT or mutant Kv11.1 channels, the decay of the tail current, measured at −70 mV (*gray line*) or −120 mV (*black line*), was fitted with a double-exponential function to obtain a τ_{fast} and τ_{slow} at each voltage (see supplemental Table 2). The relative amplitude (λ) of τ_{fast} and τ_{slow} components (*i.e.* $\lambda_{fast} = A_{\tau fast}/(A_{\tau fast} + A_{\tau slow})$ was used to assess their relative importance during the deactivation process, allowing the calculation of an adjusted τ at each voltage (see supplemental Table 2 and "Experimental procedures" for details). *B,* summary plot of the change in rate of Kv11.1 channel deactivation measured at −120 mV (*left panel*) or −70 mV (*right panel*) for each S1 alanine mutant. For WT and mutant channels, the adjusted τ was used to calculate the rate of deactivation at −120 mV ($\ln k_{deactivation,\ -120\ V}$) or −70 mV ($\ln k_{deactivation,\ -70\ mV}$) for each replicate ($n = 4$–21 as shown in supplemental Table 2), see under "Experimental procedures" for details. The $\ln k_{deactivation,\ -120\ mV\ or\ -70\ mV}$ for each replicate was then compared with the corresponding mean $\ln k_{deactivation}$ for WT, to obtain $-\Delta\ln k_{deactivation}$ (*i.e.* $\Delta\ln k_{deactivation} = \Delta\ln k_{Mt} - \Delta\ln k_{WT}^{mean}$) at each voltage. Data are shown as mean ± S.E. *Gray bars* indicate mutants that produced $-\Delta\ln k_{deactivation}$ shifts greater than ± 0.693 s^{-1} (±0.693 also indicated with *dashed lines*), which is equivalent to a doubling of the rate. * denotes mutants where the $\ln k_{deactivation}$ was found to be significantly different from WT using one-way ANOVA ($p < 0.05$). # indicates that the rate of deactivation was too slow to accurately measure at −70 mV for K407A and P426A. *C,* correlation between $-\Delta\ln k_{deactivation}$ measured at −120 mV *versus* −70 mV for WT and mutant channels. Note that K407A and P426A were not included because the slow deactivation of these mutants at −70 mV did not allow for calculated $-\Delta\ln k_{deactivation,\ -70\ mV}$. *D,* plot of the relative amplitude (λ_{fast}) of the fast component of deactivation when measured at −120 mV compared with −70 mV. At −120 mV, the kinetics of deactivation are largely a reflection of the fast component of deactivation for WT and most mutant channels (with the exception of K407A, see supplemental Table 2). At −70 mV, however, the kinetics of deactivation are largely a reflection of the slow component of deactivation for WT and some mutant channels, but the fast component plays a much larger role in many mutant channels (*i.e.* Y403A, W412A, T421A, and see supplemental Table 2). *E,* τ_{fast} for deactivation of WT, Y403A, and T421A Kv11.1 channels measured at a range of membrane potentials between −150 and −50 mV. Note that some mutants, such as T421A, dramatically alter the voltage dependence of the kinetics of deactivation.

too slow to reliably quantify and thus could not be included in the statistical analysis (*i.e.* K407A in Fig. 5*A*). The disparity between perturbations to the rate of deactivation when measured at −70 mV compared with −120 mV are highlighted in Fig. 5*C*. It is also noteworthy that at −120 mV the $\lambda_{\tau fast}$ was >0.75 for WT and all mutants except K407A (supplemental

Table 2 and Fig. 5*D*). In contrast, at −70 mV the $\lambda_{\tau fast}$ was <0.2 for WT and most unperturbed mutant channels, but this value greatly increased for mutant channels with significantly faster deactivation rates (Fig. 5*D*). At least in part, these disparities are due to an altered voltage dependence of the rate of deactivation, whereby the slope of the voltage dependence becomes much shallower (compared with WT) for most (*i.e.* T421A), but not all (Y403A), mutations that accelerate the rate of deactivation (see Fig. 5*E*).

Another unique feature of Kv11.1 channels is a uniquely fast and intrinsically voltage-sensitive C-type inactivation mechanism (8). To investigate the role of the S1 region in the C-type inactivation of Kv11.1 channels, the rates of onset of inactivation (k_{onset}) and rate of recovery from inactivation (k_{rec}) were measured using the voltage protocols shown in Fig. 6, *A* and *B, panel i*, with current traces from WT (*panel ii*) and mutant W412A (*panel iii*) shown below (Fig. 6). Time constants were derived from fits of the traces as described under "Experimental procedures." The observed rates ($k_{obs} = k_{onset} + k_{recovery}$) were then plotted against voltage to generate a chevron plot (Fig. 6*C*). The linear arms at each end of the chevron plot represent the unidirectional rate constants for the onset of inactivation (Fig. 6*C, circles*), and recovery from inactivation (*squares*). Unidirectional rate constants were then extrapolated to 0 mV ($k_{onset,\,0\,mV}$ and $k_{recovery,\,0\,mV}$), and the equilibrium constant ($K_{eq,\,0\,mV}$) for inactivation, which represents the voltage dependence of inactivation, was calculated as $k_{onset,\,0\,mV}/k_{rec,\,0\,mV}$. As shown in Fig. 6*C,* (*panel ii*), the S1 mutant W412A caused a significant depolarizing shift in the voltage dependence of inactivation, equivalent to a change in free energy of 1.25 ± 0.05 kcal mol^{-1} (n = 13). This effect was predominantly due to a perturbation in the rate of recovery from inactivation, although we did also observe a small but significant shift in the rate of onset of inactivation. In fact, W412A and F431A were the only mutants that significantly perturbed the rate of onset of inactivation (measured as $-\Delta\ln k_{onset,\,0\,mV}$) beyond the cutoff of ±0.693 s^{-1} (Fig. 6*D*). Indeed only four mutants in the S1 helix, W412A, L415A, L417A, and T421A, caused significant perturbations to the rate of recovery from inactivation ($-\Delta\ln k_{Recovery,\,0\,mV}$, Fig. 6*E*) which resulted in significant shifts in the equilibrium constant for inactivation ($\Delta\Delta G_{Eq,\,0\,mV}$, Fig. 6*F*).

For comparison, the extent of perturbation caused by pre-S1 loop or S1 helix mutations, on each of the major gating transition pathways of Kv11.1 channels, is mapped onto the homology model structure of the channel in Fig. 7. In these color maps, perturbations were normalized to the maximum change in rate or voltage dependence. Thus, perturbations to the rates of activation (Fig. 7*A*), deactivation (Fig. 7*B*), onset of inactivation (Fig. 7*C*), or recovery from inactivation (Fig. 7*D*) were normalized to the maximal perturbation across all four parameters (*i.e.* the perturbation to rate deactivation caused by K407A). Similarly, the voltage dependence of activation (Fig. 7*E*) and inactivation (Fig. 7*F*) was normalized to the maximal perturbation from these two parameters (*i.e.* the perturbation to activation caused by Y403A channels); *white* represents no perturbation compared with WT, *darker red* represents the maximal perturbation in the positive direction (representing a slower rate or a depolarizing shift in the voltage dependent equilibrium), and *darker blue* represents the maximum perturbation in the negative direction (representing a faster rate or a hyperpolarizing shift in the voltage dependent equilibrium). It is clear from these color maps that the largest observed perturbations were to the rate of deactivation and the voltage dependence of channel activation. In both cases, the most perturbing mutations are located in the pre-S1 loop, just prior to the N-terminal end of the S1 helix, as well as throughout the S1 helix. Although these highly perturbing mutations do not necessarily map to a single face of the helix, it appears that the side chains of the most perturbing residues face toward either the S2 or S4 helices within the same subunit of the Kv11.1 channel.

Both the activation and deactivation pathways were greatly perturbed by S1 residue mutations. However, as shown in Fig. 8*A*, there was no degree of correlation between mutation-induced perturbations to the rate of deactivation and either the voltage-dependent equilibrium of activation (R^2 = 0.03) or the rate of activation (R^2 = 0.01), implying that, at least in Kv11.1 channels, the deactivation transition pathway (open-to-closed) is not simply the reverse of the activation transition pathway (closed-to-open). There was also no correlation between mutant-induced perturbations to the voltage-dependent equilibrium of activation and the voltage-dependent equilibrium of inactivation (R^2 = 0.00, Fig. 8*B*) indicating that the voltage-sensing process in these two gating transitions is distinct for Kv11.1 channels.

Effect of clinical LQTS2 causing mutations in the S1 region

Our data demonstrate that the mutation of residues in the pre-S1 loop or the S1 helix can differentially perturb all aspects of Kv11.1 channel gating, suggesting that these regions are critical regulators of the finely tuned state occupancy of the channels at different membrane potentials. A number of LQTS2-causing mutations within the region of the pre-S1 loop and S1 helix of Kv11.1 channels have been identified in the International LQT registry, namely I400N, H402R, W410S, Y420C, T421M, and S428L (9). Thus, we sought to examine whether these clinically relevant Kv11.1 channel mutants would exhibit altered phenotypes. We explored two common types of dysfunction caused by LQTS2-associated mutations: reduced expression of the Kv11.1 channel protein at the membrane and altered function of the expressed channels (see under "Discussion" for limitations of this analysis).

First, we examined whether LQTS2 mutations in the S1 region alter protein expression at the membrane. Western blotting data performed on mammalian HEK293 cells transiently transfected with mutant or WT cDNA demonstrates a reduced expression associated with all six pre-S1/S1 mutations (see Fig. 9), indicating that the S1 region may also be important for proper folding and/or trafficking of channel protein.

Further analyses of the function of these six LQTS2-associated mutant channels when expressed in *Xenopus* oocytes demonstrate that several mutants perturb multiple gating transition pathways (Fig. 10, *A–D,* and supplemental Tables 1–3). For example, the pre-S1 mutation H402R caused a considerable and significant hyperpolarizing shift in the voltage dependence of activation, an accelerated rate of channel deactivation, and a

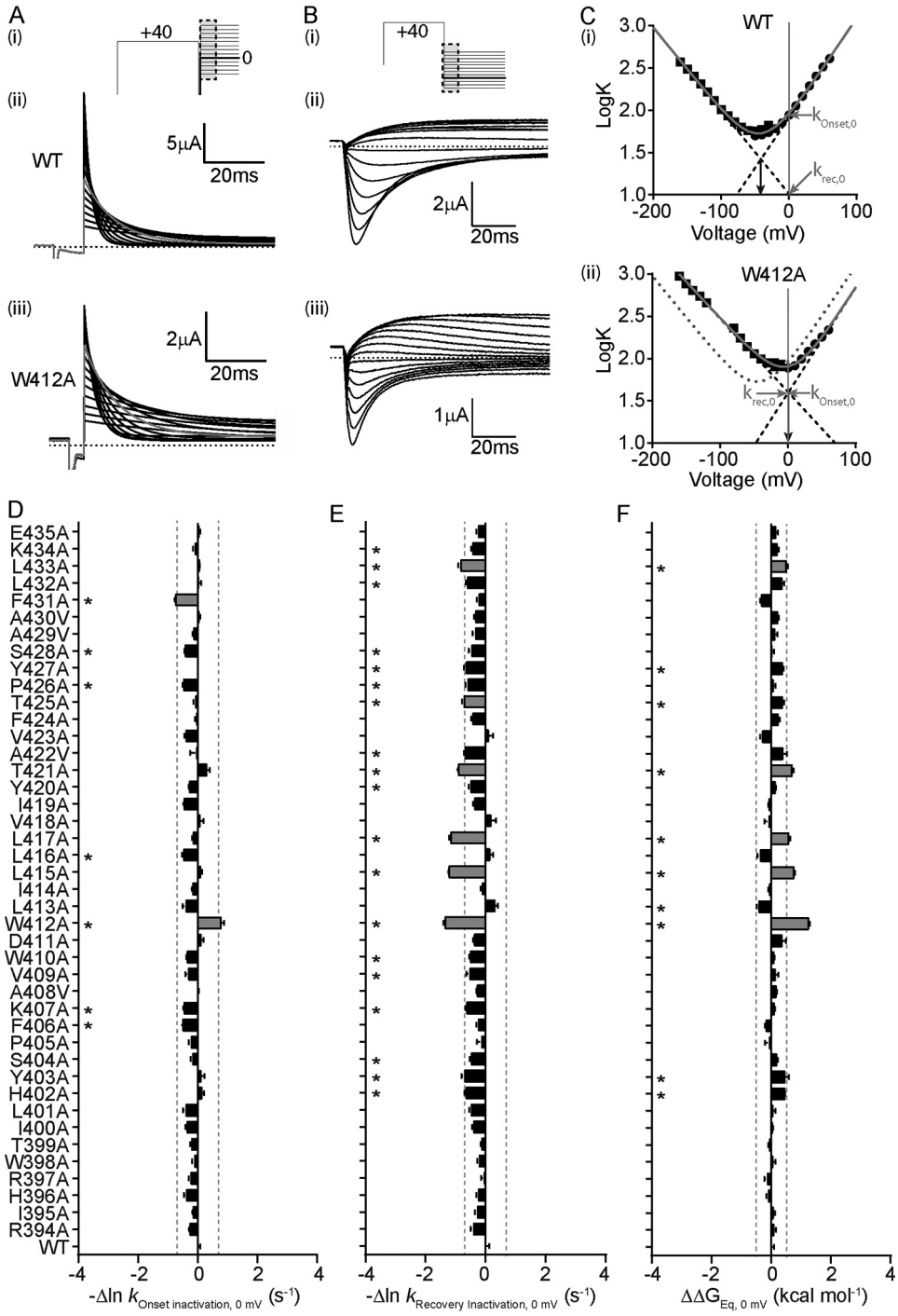

Figure 6. S1 helix plays only a minor role in regulating the C-type inactivation of Kv11.1 channels. *A* and *B,* voltage protocols (*panel i*) used to measure the kinetics of onset of inactivation (*A*) and the kinetics of recovery from inactivation (*B*), with key regions for the measurement of current highlighted in *gray*. Typical families of currents measuring the rates of onset of inactivation (*A*) and rates of recovery from inactivation (*B*) for WT (*panel ii*) and W412A (*panel iii*) Kv11.1 channels. Kinetics for the onset of inactivation (*A*) were obtained by fitting the decay in current to a single exponential function to obtain τ_{onset} at a range of voltages between +60 and −60 mV. Kinetics for the recovery from inactivation (*B*) were obtained by fitting the hooked tail current to a double-exponential function, and selecting the τ that corresponds to the initial rising phase of the hook, to obtain $\tau_{recovery}$ at a range of voltages between −20 and −160 mV. *C,* chevron plots of the logarithm of the observed rates for onset of (*closed circles*) and recovery from (*closed squares*) inactivation for WT (*panel i*) and W412A (*panel ii*) channels, plotted against voltage. *Solid gray lines* are a fit of Equation 1 (see "Experimental procedures"), whereas the *dashed gray* line in *panel ii* indicates $k_{obs,\ mV}$ for WT channels to aid comparison. *Dashed black lines* indicate the derived unidirectional rate constants for the onset of (k_{onset}) and recovery from ($k_{recovery}$) inactivation, with values at 0 mV indicated by *gray arrows*. The equilibrium constant for inactivation (K_{eq}) at 0 mV was calculated by $K_{eq,\ 0} = k_{inact,\ 0}/k_{rec,\ 0}$. Values of $k_{inact,\ 0\ mV}$, $k_{recovery,\ 0\ mV}$, and $K_{eq,\ 0\ mV}$ are given for WT and each mutant in supplemental Table 3. *Downward arrows* indicate the voltage at which $k_{onset,\ 0\ mV} = k_{recovery,\ 0\ mV}$, which provides an estimate of the voltage at which half the maximal number of channels are inactivated. *D–F,* summary plots of the change in the rate for the onset of inactivation ($-\Delta\ln k_{onset,\ 0\ mV}$, *D*), or recovery from inactivation ($-\Delta\ln k_{recovery,\ 0\ mV}$, *E*), or the change in free energy for the equilibrium ($\Delta\Delta G_{Eq,\ 0\ mV}$, *F*) of inactivation for each S1 alanine mutant compared with WT (see "Experimental procedures" for calculation of $-\Delta\ln k$ and $\Delta\Delta G$ values). Data are shown as mean ± S.E. *Gray bars* indicate mutants that produced $-\Delta\ln k_{Deactivation}$ shifts greater than ± 0.693 s^{-1} or $\Delta\Delta G$ shifts greater than ± 0.5 kcal mol^{-1} (also indicated with *dotted lines*). * denotes mutants where the ln*k* or ΔG were found to be significantly different from WT using one-way ANOVA ($p < 0.05$).

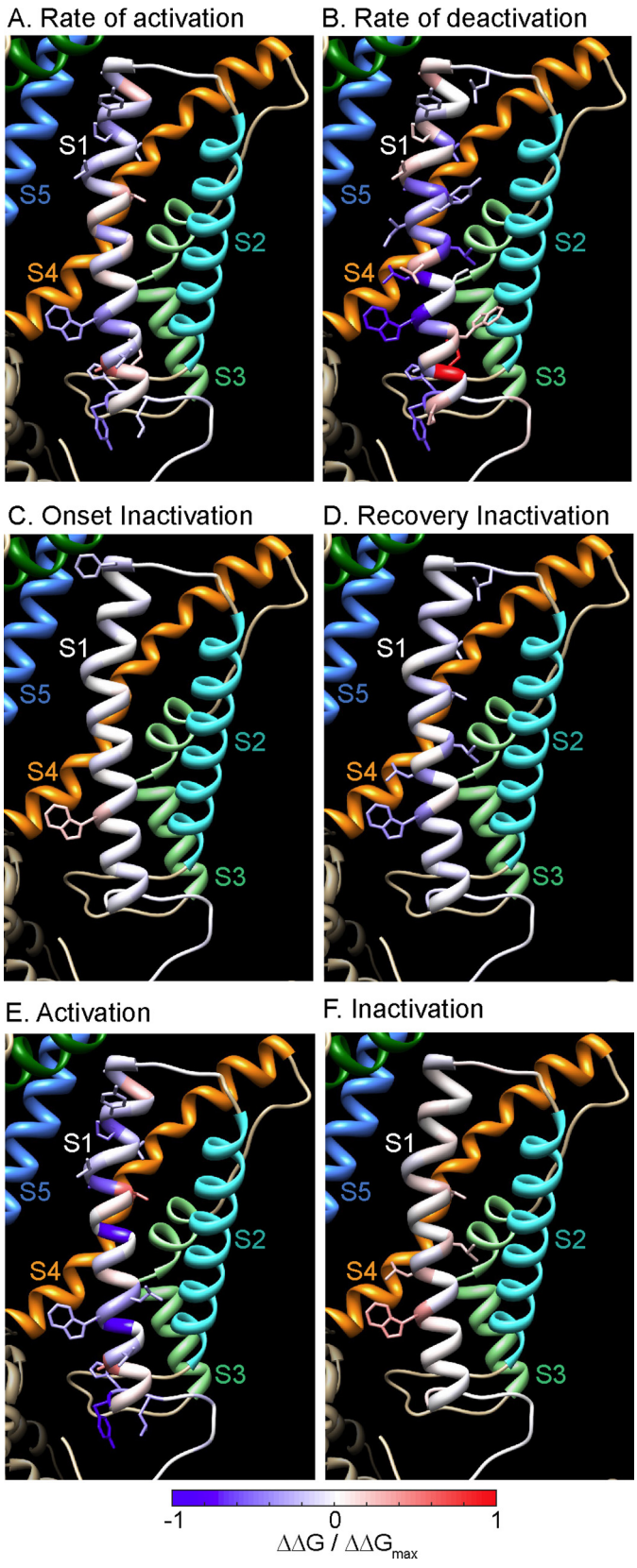

Figure 7. Comparison of the effect of S1 mutants on the gating processes of Kv11.1 channels. *A–F,* color maps comparing perturbations to the energetics of all major gating processes of Kv11.1 channels in response to single residue mutations in the S1 helix. The homology model of the Kv11.1 channel is based on the cryo-EM structure of the rEAG channel (50). The unperturbed S1 helix is colored *white*, whereas other helices are colored as follows: S2 (*cyan*), S3 (*light green*), S4 (*orange*), S5 (*blue*), and the pore helix (PH, *dark green*). Perturbations to the rate of activation (*A*), the rate of deactivation (*B*), the rate of onset of inactivation (*C*), the rate of recovery from inactivation (*D*), the voltage dependence of activation (*E*), and the equilibrium of inactivation (*F*) were all calculated from the relevant $-\Delta\ln k$ or $\Delta\Delta G$ (*versus* WT) values shown in Figs. 3–6 (see under "Experimental procedures" for details). $-\Delta\ln k$ values of rates (*A–D*) were normalized to the maximal perturbation from all four categories combined, whereas the $\Delta\Delta G$ values of equilibria (*E* and *F*) were normalized to the maximal perturbation from these two categories combined. Color coding is shown below, where *red* indicates maximal perturbation in the positive direction (*i.e.* slower rate or a depolarizing shift in the voltage equilibria), and *blue* indicates the maximal perturbation in the negative direction (*i.e.* faster rate or a hyperpolarizing shift in the voltage equilibria). Side chains are shown only for those mutants where perturbations were significant (ANOVA, $p < 0.05$) and had $-\Delta\ln k$ values $> \pm 0.693$ s^{-1} (equivalent to a doubling or halving of the rate) or $\Delta\Delta G$ values $> \pm 0.5$ kcal mol^{-1}.

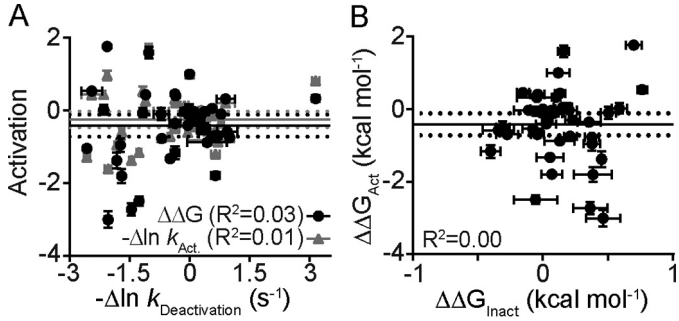

Figure 8. Lack of correlation between S1 mutant-induced perturbations to Kv11.1 gating parameters. *A* S1 mutant-induced perturbations to the rate of deactivation plotted against the perturbations to the energetics of the voltage-dependent equilibrium of activation (*black circles*), the rate of activation (*gray triangles*). *B*, S1 mutant-induced perturbations to voltage dependent equilibria of activation plotted against the voltage-dependent equilibrium of inactivation. Data were fitted with a linear function, and the R^2 goodness of fit values are given in *parentheses*.

depolarizing shift in the voltage dependence of inactivation. Conversely, the S1 mutation T421M caused an opposite depolarizing shift in the voltage dependence of activation, while also showing fast deactivation and dramatically reduced inactivation (Fig. 10, *A–D*). One of the least perturbing LQTS2 mutants was W410S, which had no effect on activation or inactivation parameters but did slow the rate of channel deactivation, such that it was not possible to accurately quantify at −70 mV. A slowed rate of deactivation measured at −120 mV was observed and quantified for W410S, as shown in supplemental Table 2.

We hypothesized that the considerable perturbations to the gating transitions of Kv11.1 channels caused by the pre-S1/S1 helix LQTS2 mutations would result in drastically altered physiological phenotypes. As shown in Fig. 10*E*, we examined the amount of Kv11.1 current passed by each mutant channel during a mimic of a cardiac action potential (*panel i*) and in response to premature depolarizations given during or after the repolarization phase of the action potential (*panel ii*). It can clearly be seen that the perturbations caused by most LQTS2-causing S1 mutations are sufficient to dramatically alter the functional phenotype. For example, the altered activation and inactivation properties of the pre-S1 H402R mutant result in a considerable spike in current during the early plateau phase of an action potential. Although the amount of H402R-Kv11.1 current passed during the repolarization phase of the action potential appears relatively normal, the amount of protective

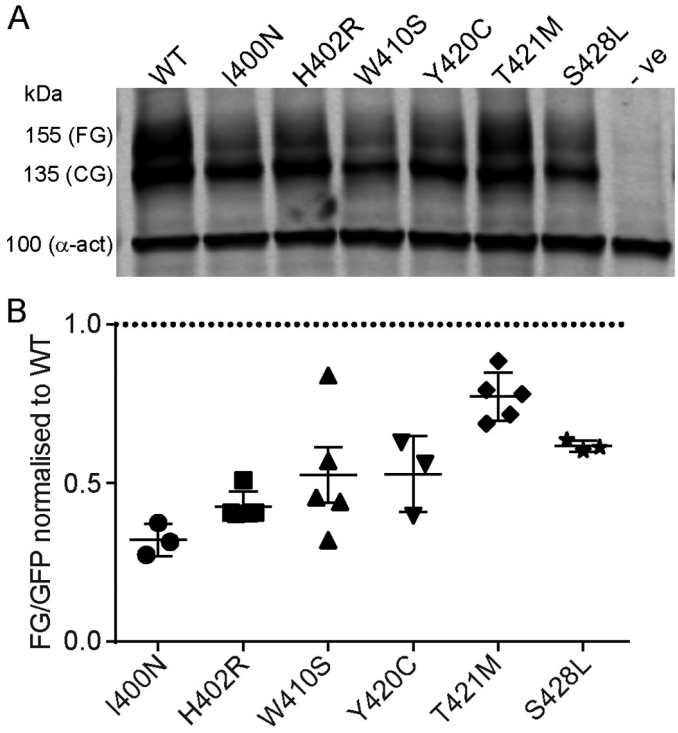

Figure 9. LQTS2 mutations in the S1 region alter the expression of Kv11.1 channels. *A,* example Western blot for WT Kv11.1 and LQTS2-associated S1 region mutants as follows: I400N, H402R, W410S, Y420C, T421M, and S428L. All constructs co-expressed GFP and were transiently transfected into HEK293 cells for 48 h prior to Western blotting. Fully glycosylated protein bands (*FG*; ~155 kDa) represent channel protein at the membrane, and core-glycosylated protein bands (*CG*; ~135 kDa) represent non-membrane channel protein. α-actin in (~100 kDa) was used as a loading control. *B,* summary box and *whiskers* plot quantifying the density of the FG band, normalized to GFP to control for variations in transfection efficiency. FG/GFP for mutant is shown relative to WT Kv11.1 protein (*i.e.* WT = 1). Data are shown as mean ± S.E., with *symbols* indicating individual replicates (n = 3–5).

current passed in response to premature depolarizations was drastically reduced, largely due to the much faster rate of deactivation. The S1 mutation T421M also dramatically reduced the amount of protective current elicited in response to premature depolarizations, similarly due to the fast deactivation phenotype of this mutant. The altered current phenotypes of all six mutant channels are summarized in Fig. 10*F*, using a color map of Kv11.1 amplitudes taken in 20-ms intervals during the step phase (the action potential plateau), the ramp repolarization phase, and in response to premature stimuli. In the color map of Fig. 10*F*, *white* represents WT-like current, progressively *darker blue* represents reduced current amplitudes, and progressively *darker red* represents increased current amplitudes compared with WT. Clearly, many of the LQTS2-associated S1 region mutations have altered functional phenotypes that, when combined with the perturbed expression phenotypes, would lead to a reduced repolarizing current that would *per se* reduce the QT interval on a body surface electrocardiogram and predispose patients to arrhythmia. On top of this, many of the mutants result in dramatically reduced protective currents in response to premature depolarizations, thereby increasing their pro-arrhythmic potential.

Discussion

In this study, we used NMR spectroscopy, homology modeling, and electrophysiological recordings to examine the structural extent and functional properties of the S1 helix in Kv11.1 channels. Structural analysis and homology modeling data suggest that the S1 helix begins at Pro-405 and extends around seven helical turns to Phe-431. The S1 helix is likely flanked at the N- and C-terminal ends by unstructured loops, termed the pre-S1 loop and the S1-S2 linker. The functional analysis using scanning mutagenesis suggests that the pre-S1 loop residues His-402 and Tyr-403 play an important role in regulating the voltage dependence of channel opening, as well as regulating the slow closure that is an important feature of Kv11.1 channels. Multiple residues within the S1 play an important role in fine-tuning the voltage dependence of activation, regulating slow deactivation, and to a lesser extent modulating C-type inactivation transitions of Kv11.1 channels. Finally, we show that clinically identified mutations located in the pre-S1 or S1 helix of Kv11.1 channels, which have been linked to long QT syndrome type 2, would lead to altered physiological phenotypes due to the combined effect of reduced Kv11.1 channel expression and altered gating properties.

Revealing the extent of the S1 helix in Kv11.1 channels

To date, bioinformatic predictions of the extent of the S1 helix in Kv11.1 channels have varied considerably (28, 35, 46–49). The N-terminal end of the S1 helix has been reported as anywhere from Ile-395 (47) to Asp-411 (35), a span equivalent to more than four helical turns. Similarly, the C-terminal end of the S1 helix has been reported from Ile-419 (47) to Glu-435 (35). Primarily, this is because the pairwise and global sequence alignments demonstrate low sequence homology for the S1 segment of Kv11.1 channels compared with other Kv family members, with identity ranging from 5.9 to 19% and similarity ranging from 28 to 44% (28, 35, 46–49). NMR spectroscopy and Gd^{3+} suppression investigations of an isolated, extended, S1 region peptide suggest that the transmembrane helical segment of S1 spans at least from Trp-410 to Leu-432.

Using a recently published cryo-EM closed-state structure of rat EAG1 (50), in which the S6 activation gate is closed but the voltage sensor domain is in an "activated" conformation (activated-state model), we built a homology model of the Kv11.1 channel that is shown in Fig. 2. This homology model suggests that the S1 helix begins five residues prior to the NMR prediction: at Pro-405 *versus* Trp-410 and finishes at Phe-431, which is similar to the Leu-432 found in our NMR studies. Given that the NMR analysis was performed on an isolated peptide, and within an artificial micelle environment, one would not necessarily expect it to exactly match the exact boundaries of the S1 transmembrane in an intact channel, although they do broadly agree, especially at the extracellular end of the S1 segment.

In the NMR analyses, a large positive chemical shift index at Thr-425 and Pro-426 suggests a potential kink or break in the S1 helical segment around this location. This would not be an unreasonable suggestion, given that proline residues are known to cause kinks in helices (59). In the Kv11.1 channel homology model there appears to be a kink in the S1 helix around residues

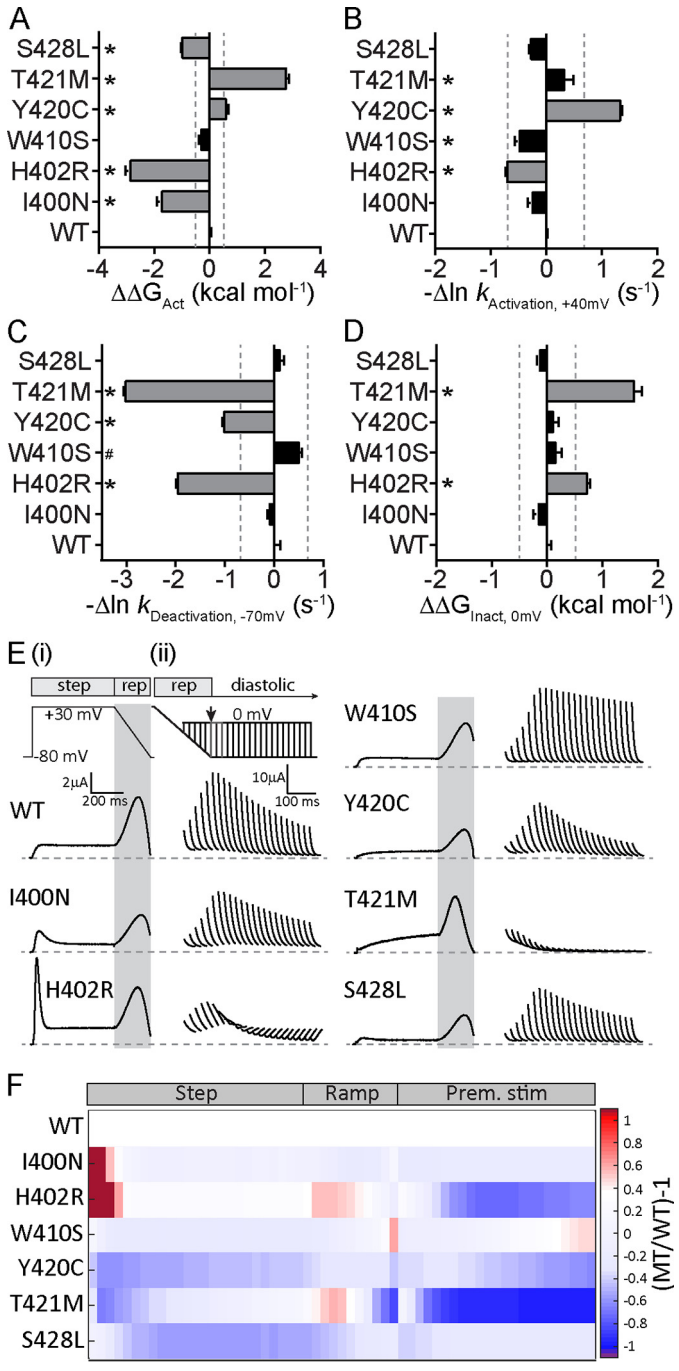

Figure 10. Altered functional phenotypes of Kv11.1 channels caused by LQTS2 mutations in the S1 region. *A–D,* summary plots of the change in the energetics of the voltage dependence of activation ($\Delta\Delta G_{Act}$; *A*), the rate of activation measured at +40 mV ($-\Delta\ln k_{activation,\ +40\ mV}$; *B*), the rate of deactivation measured at −70 mV ($-\Delta\ln k_{deactivation,\ -70\ mV}$; *C*), or equilibrium of inactivation ($\Delta\Delta G_{Inact,\ 0\ mV}$, *D*) for each LQTS2-associated S1 mutant compared with WT (see "Experimental procedures" for calculation of $-\Delta\ln k$ and $\Delta\Delta G$ values). # denotes that the rate of deactivation at −70 mV was too slow to reliably measure for W410S mutant channels (data at −120 mV is given instead and in supplemental Table 2). Data are shown as mean ± S.E. *Gray bars* indicate mutants that produced $-\Delta\ln k$ shifts greater than ± 0.693 s^{-1} or $\Delta\Delta G$ shifts greater than ±0.5 kcal mol^{-1} (also indicated with *dotted lines*). * denotes mutants where the ln*k* or Δ*G* were found to be significantly different from WT using one-way ANOVA ($p < 0.05$). *E, panel i,* ventricular action potential "step-ramp" voltage protocol (see "Experimental procedures") designed to examine the current phenotype ($I_{Kv11.1}$) passed by WT or LQTS2-associated S1 mutant channels during a ventricular action potential. Below are typical families of currents from WT or LQTS2 associated mutant channels in response to the step-ramp protocol. Note that WT Kv11.1 channels activate slowly and inactivate rapidly (C⟶O⟶I), so minimal $I_{Kv11.1}$ is observed during the +30-mV step pulse. Channels rapidly recover from inactivation (I⟶O) during the repolarization ramp allowing a large increase in $I_{Kv11.1}$, which reaches peak amplitude about halfway through repolarization. The decline in $I_{Kv11.1}$ during terminal repolarization is due to a decrease in driving force rather than channel deactivation, which occurs slowly during the diastolic interval. Repolarizing $I_{Kv11.1}$ is defined as the area highlighted in *gray*. *Panel ii,* premature depolarizations (steps to 0 mV for 40 ms) were delivered during the step-ramp protocol shown in *panel i*, starting 120 ms after the start of the ramp and continuing at 20-ms intervals in 23 successive sweeps, finishing 560 ms after the start of the repolarizing ramp. Below are typical $I_{Kv11.1}$ peaks measured from WT or LQTS2 mutants channels at each premature depolarization time point by fitting the $I_{Kv11.1}$ at 0 mV with a single exponential function and extrapolating back to the start of the voltage step. The envelope of peak current spikes for WT-$I_{Kv11.1}$ shows a typical biphasic profile, peaking 240 ms after the start of the repolarizing ramp. Both the repolarizing $I_{Kv11.1}$ and the protective $I_{Kv11.1}$ phenotypes were altered in the presence of LQTS2-associated mutations in the pre-S1 or S1 region. *F, color map* comparing the amplitude of $I_{Kv11.1}$ passed by WT and LQTS2-associated pre-S1/S1 mutant channels at 20-ms intervals during the plateau and repolarizing ramp phases of the step-ramp protocol, as well as in response to premature stimuli. *White* represents WT-like levels of $I_{Kv11.1}$, and *darker red* represents progressively increased $I_{Kv11.1}$ compared with WT; *darker blue* represents progressively less $I_{Kv11.1}$ compared with WT, and *purple* denotes inward $I_{Kv11.1}$.

Phe-424–Thr-425–Pro-426, which is consistent with the NMR data. A more pronounced break and kink is observed in the crystal structure of the Kv1.2/2.1 chimera, at positions Thr-184–Leu-185–Pro-186 (37). In the functional studies of Kv11.1 channels, mutation of residues Thr-425 or Pro-426 were moderately perturbing to both the voltage dependence and kinetics of channel activation, as well as to the kinetics of deactivation, but did not alter the C-type inactivation properties of the channel, suggesting that this kink may be functionally important in mediating transitions between the open and closed conformations of Kv11.1 channels.

In Kv11.1 channels, Colenso *et al.* (35) used a molecular dynamics approach to identify a possible interaction between residues at the top end of the S1 helix, Leu-432 and Leu-433, and residue side chains in the pore helix, at Tyr-611 and Val-612. A similar interaction has been proposed to be structurally and functionally important as one of two critical interfaces between the voltage sensor and pore domains of two other Kv channels (34, 36). In the homology model, both Leu-432 and Leu-433 lie just outside of the S1 helix in the S1-S2 linker. In our study, mutation of these residues did not alter activation properties of the channel, although L433A did produce a small but significant perturbation to the rate of deactivation and steady-state inactivation. These data suggest that the extracellular end of S1 may not be as critical for maintaining the normal gating of Kv11.1 channels compared with other voltage-gated K^+ channels.

Functional role of the S1 helix in Kv11.1 channels

To probe the contribution of each S1 helix residue, we used alanine-scanning mutagenesis. Alanine was chosen because it would remove the interactions of the native functional group in any larger side chain amino acids, while causing minimal structural perturbation. When mapped onto the activated-state homology model of Kv11.1, the most perturbing mutations to the voltage dependence of activation (*i.e.* the closed-to-open transition) were spread throughout the S1 helix, although many had side chains that were in close proximity to either the S2 helix or the S4 helix of the voltage sensor domain from the same subunit

(see Fig. 7). This suggests that the S1 helix likely forms a complex network of intra-subunit interactions with these two helices. In Kv11.1 channels, as well as in many other Kv family members, negatively charged residues in the S1, S2, and S3 helices are thought to form charge-charge interactions with positively charged residues within the S4 helix (28, 29, 31, 49). This network of charge paired interactions stabilizes the S4 voltage sensor and fine tunes the voltage sensitivity of channel activation. In the S1 helix, the negatively charged residue Asp-411 has been reported to interact with the positively charged S4 helix residue Lys-438 to stabilize the closed state of the channels (29). Our findings would support this proposed interaction. However, our data would also suggest that this network of intra-subunit interactions is not just limited to charge pairing but that the S1 may form a complex and diverse network of contacts with the S2 and S4 helices of the voltage sensor domain. For instance, in addition to D411A, there were 13 other alanine mutants in the S1 helix that significantly perturbed the voltage dependence of channel activation. The homology model suggests that the side chains of at least three of these residues (Val-418, Thr-421, and Thr-425) directly face the S4 helix of the same subunit. Thr-421 contains a polar side chain that could form interactions with negatively charged residues in the S2 helix and/or positively charged residues in the S4 helix. Mutation T421A, as well as the clinical LQTS2 mutation T421M (see Fig. 10) (16), both caused a profound depolarizing shift in the voltage dependence of activation, suggesting that interactions involving Thr-421 may stabilize the activated state of the channel.

Many S1 mutations perturb the rate of channel deactivation

In the functional analyses of the S1 helix, we observed significant perturbations to the kinetics of channel deactivation (the open-to-closed transition) for 19/27 mutants. Twelve of the 19 perturbing mutations resulted in faster rates of channel closure, whereas only seven caused a slowing of deactivation. The fact that more mutants accelerate, rather than slow, the rate of deactivation may not be surprising as this transition is already more than 10-fold slower in Kv11.1 channels than in most other members of the Kv family (8). Most of these mutations were perturbing to deactivation measured at the physiological voltage of −70 mV but not when measured at −120 mV. The principal reason for this difference appears to be that many of the perturbing mutants reduce the steepness of the voltage dependence of the kinetics of deactivation (see Fig. 5*E*).

Interestingly, for the S1 mutants we examined, there was no correlation between the perturbations to the rate of deactivation and either the voltage dependence of activation or the rate of activation (see Fig. 8*A*). The major implication from these data is that in Kv11.1 channels the open-to-closed transition (deactivation) is not a simple reversal of the closed-to-open transition (activation), but instead deactivation involves transition through a distinct set of short-lived intermediate states. Previous work in which N-terminal truncation of Kv11.1 caused perturbations to channel deactivation, but not activation, also supports this notion (27). Because there were more S1 mutants that accelerated the rate of deactivation, at least at physiological voltages, compared with those that perturbed the rate of activation, it may be that the S1 helical segment acts as an allosteric modulator, involved in important interactions that stabilize intermediate states of the open-to-closed transition and thus contribute to the slow deactivation of WT Kv11.1 channels. A notable exception to this trend is that of K407A, a mutation at the intracellular end of the S1 helix that dramatically slowed the rate of Kv11.1 channel closure.

Limitations of homology model

It should be noted that our homology model is based on the structure of the rat EAG channel, which was captured with the activation gate closed but with the voltage sensor likely in the "up" or activated conformation (50). There are currently no structures of any Kv channel, which have the voltage sensor in the "down" or relaxed conformation. Thus the potential interactions we discussed above, based on our homology model, reflect only a snapshot in time during the closed-open transition.

Role of S1 in channel inactivation

In many Kv channels, the voltage dependence of channel inactivation is linked to the voltage dependence of activation, whereas in Kv11.1 channels the C-type inactivation process may be intrinsically voltage-dependent (8, 24). Our data identified only four mutants in the S1 helix, W412A, L415A, L417A, and T421A, that caused significant perturbations to the equilibrium for inactivation, as measured from the forward (onset) and reverse (recovery) rates for inactivation. In three out of four mutants, with the exception being W412A, perturbation to the equilibrium was primarily a consequence of faster rates of recovery from inactivation and not due to altered rates of onset of inactivation. This picture starkly contrasts with what was observed for the voltage dependence of activation (see Figs. 7 and 8), where perturbing positions were distributed throughout the S1 helix. This supports the notion that activation and inactivation are not coupled in Kv11.1 channels.

Role of the pre-S1 loop in Kv11.1 channels

Recent protein structures of a range of ion channels have identified the presence of a short helical segment just before the S1 helix, termed the pre-S1, S0, or S0′ helix. This segment is postulated to play a role in biogenesis, protein folding, and gating of these channels (37–45). Our NMR spectroscopy and Gd^{3+} suppression data did not support the presence of a pre-S1 helix in Kv11.1 channels. Furthermore, the Kv11.1 homology model that we created from the structure of the rat EAG channels suggests that the pre-S1 is an unstructured loop. Nevertheless, the pre-S1 loop in Kv11.1 channels is functionally important. Mutation to alanine of three individual pre-S1 residues, Ile-400, His-402, and Tyr-403, caused significant hyperpolarizing shifts in the voltage dependence of channel activation, as well as accelerating the kinetics of both activation and deactivation. In particular, Y403A caused some of the largest perturbations to these gating parameters that we observed across all mutants studied. Clinical LQTS2-associated mutations I400N and H402R also dramatically reduced expression and altered the gating properties of the Kv11.1 channels, further indicating that the pre-S1 loop is an important functional domain. It is

notable that the perturbations to function caused by mutations in the pre-S1 loop, notably a much faster deactivation, are similar to those seen with mutations to the N-terminal Per-Arnt-Sim domain and the C-terminal C-linker and cNBHD (20, 22, 60). Furthermore, it has been suggested that this intracellular complex interacts with the intracellular end of the voltage sensor domain (61). Thus, although the pre-S1 loop appears to be unstructured in Kv11.1 channels, it is still possible that it interacts with the complex of intracellular domains that modulate the slow deactivation phenotype in Kv11.1 channels with the pre-S1 loop residues His-402 and Tyr-403 being key contributors to this process.

Effect of clinical LQTS2 causing mutations in the S1 region

Of the six LQTS2-associated mutants we examined, located in the pre-S1 loop (I400N and H402R) or the S1 helix (W410S, Y420C, T421M, and S428L), all showed some degree of reduction in membrane expression of the channel protein (Fig. 9), as well as perturbation to at least one or more gating transitions (Fig. 10, *A–D*). As a consequence, these S1 region mutations would reduce both the action potential repolarizing current passed by Kv11.1 channels in cardiac myocytes and/or the current passed in response to premature depolarizations (Fig. 10, *E* and *F*), and so likely to increase the risk of cardiac arrhythmias.

For the LQTS2 mutations, we assessed two common types of dysfunction: altered protein expression at the membrane and altered function (*i.e.* gating) of the expressed Kv11.1 channels. For protein expression estimates, a Western blotting assay of WT and mutant channel protein was performed using transiently transfected mammalian HEK293 cells incubated at 37 °C. This is preferable to the *Xenopus* oocyte expression system for expression analysis because low temperature (17 °C) incubation of oocytes allows for the rescue of expression of some mutations (8). Conversely, we exploited the rescued expression in oocytes to our advantage by measuring the gating properties of mutant channels in the oocyte expression system. These electrophysiological recordings were undertaken at room temperature, rather than at physiological temperature (37 °C), which is known to slow gating kinetics (62). Even so, it is likely that the relative differences between WT and mutants will be similar in different expression systems, as shown previously for mutations F29L (14, 18, 63) and R56Q (14, 63–65).

Limitations of LQTS2 phenotyping

It is important to note that neither mammalian HEK293 cells nor *Xenopus* oocytes contain the same complement of accessory proteins found in cardiac myocytes. Also, effects related to phosphorylation, or regulation by other signaling pathways, have not been taken into account. These limitations, if anything, will result in our underestimating the functional defects associated with the S1 mutations.

Conclusions

Our study refines the extent of the S1 helix in Kv11.1 channels and demonstrates that the S1 helix and the pre-S1 loop are important structural factors in the normal expression and function of Kv11.1 channels. Clinical LQTS2 mutants that perturb the pre-S1 loop or S1 helix can lead to disruption of the finely tuned properties of Kv11.1 channels, reducing the action potential repolarizing current passed by Kv11.1 channels in cardiac myocytes, as well as the current passed in response to premature depolarizations, thereby predisposing patients to increased risk of electrical arrhythmias and sudden cardiac death.

Experimental procedures

Peptide synthesis

The 45-residue Kv11.1 S1 peptide (RIHRWTILHYSPFKAVWDWLILLLVIYTAVFTPYSAAFLLKETEE) was commercially synthesized by Mimotopes (Melbourne, Australia).

Nuclear magnetic resonance (NMR) spectroscopy

Samples for NMR spectroscopy consisted of 1 mM of the S1 peptide dissolved in 350 μl of 90:10, H_2O/D_2O, v/v, containing 100 mM deuterated SDS (Cambridge Isotope Laboratories, Andover, MA). All of the experiments were performed on a Bruker Avance III 800 MHz narrow-bore NMR spectrometer (Bruker, Karlsruhe, Germany) equipped with TCI cryoprobe with a sample temperature of 35 °C. Raw data were processed using TopSpin™ (Bruker, Karlsruhe, Germany) and analyzed with SPARKY (T. D. Goddard and D. G. Kneller, University of California at San Francisco).

Gadolinium (Gd^{3+}) is a paramagnetic relaxation agent that suppresses ^1H signals from residues located outside of the micelle environment (51). Gadolinium/diethylenetriaminepentaacetic acid/bismethylamide (a gift from Dr. Klaus Zangger, University of Graz, Graz, Austria) was introduced to the sample at a concentration of 2 mM. The two-dimensional (2D) experiments that were performed before and after the addition of the relaxation agent, Gd^{3+}, included total correlation spectroscopy (TOCSY (66)) with Malcolm Levitt's composite-pulse decoupling sequence spin-lock periods of 90 ms, and nuclear Overhauser enhancement spectroscopy (NOESY (67)) with mixing time of 150 ms.

Residue assignments were made according to the standard protocol from 2D TOCSY and NOESY experiments. The 1D proton spectrum was acquired before and after 2D TOCSY and NOESY experiments to ensure that the signal intensity had not changed due to loss of integrity of the S1 peptide. To analyze the effect of the relaxation agent, the peak intensities of ^1H resonances from the NOESY experiments were quantified for each residue before and after the addition of the Gd^{3+} agent. Data are expressed as the fraction of ^1H signal remaining after addition of Gd^{3+} (*i.e.* post-Gd^{3+}/pre-Gd^{3+}). Thus, a value of 1 denotes no suppression of the ^1H signal by Gd^{3+} and indicates that the corresponding residue is likely to be located within the micelle environment (*i.e.* within the transmembrane helix), whereas a value of 0 denotes complete suppression by Gd^{3+} and strongly suggests the corresponding residue lies outside of the micelle environment (*i.e.* outside of the transmembrane helix).

Bioinformatics/homology model generation

A Kv11.1 channel homology model was generated from the structure of rEAG (50), Protein Data Bank code 5K7L, using

Swiss PDB Viewer (68) and optimized using SWISS-MODEL Workspace (69, 70).

Molecular biology

Kv11.1 cDNA (gift from G. Robertson, University of Wisconsin, Madison) was subcloned into a pBluescript vector containing the *Xenopus laevis* β-globin gene. Mutagenesis was performed using QuikChange (Stratagene Inc.), according to the manufacturer's protocols. Residues 394–435 were individually mutated to alanine (or alanine to valine). Mutations were confirmed by DNA sequencing. Plasmids were linearized using BamHI-HF (New England Biolabs), and cRNA was transcribed *in vitro* using an mMessage mMachine T7 kit (Ambion) according to the manufacturer's protocols.

Electrophysiology

All experiments were approved by the Garvan/St. Vincent's Animal Ethics Committee (approval identifier 14/30). Female *X. laevis* frogs were purchased from Nasco (Fort Atkinson, WI). Following anesthetization in 0.17% w/v tricaine (Sigma, Castle Hill, New South Wales, Australia), the ovarian lobes were removed through a small abdominal incision. The follicular cell layer was removed by an ~2-h digestion with 1 mg/ml collagenase A (Roche Diagnostics, Castle Hill, New South Wales, Australia) in Ca^{2+}-free ND96 solution containing the following (mM): NaCl 96, KCl 2, $MgCl_2$ 1.0 and HEPES 5 (pH adjusted to 7.5 with NaOH). After rinsing with ND96 (as above, plus 1.8 mM $CaCl_2$), stage V and VI oocytes were isolated and stored at 17 °C in tissue culture dishes containing ND96 supplemented with 2.5 mM pyruvic acid sodium salt and 10 $\mu g/ml^{-1}$ amikacin.

X. laevis oocytes were injected with cRNA and incubated at 17 °C for 12–48 h prior to electrophysiological recordings. Two-electrode voltage-clamp experiments were performed at room temperature using a GeneClamp 500B amplifier connected to a PC via a Digidata 1440A AC/DC converter. Cells expressing alanine scan mutations were perfused with ND96 solution containing the following (in mM): NaCl 96, KCl 2, $CaCl_2$ 1.8, $MgCl_2$ 1.0 and HEPES 5, pH adjusted to 7.5 with NaOH. For LQTS2-associated mutations, cells were perfused with ND96 solution in which the KCl was raised to 4 mM, to better mimic physiological concentrations, whereas NaCl was reduced to 94 mM. Glass microelectrodes were filled with 3 M KCl and had tip resistances of 0.3–1.0 megohms. All data are shown as means ± S.E. of mean for n experiments, where n denotes the number of oocytes studied for each construct. Data acquisition and analysis were performed using pCLAMP10.4, Excel, and Graphpad Prism 6 software.

Voltage-clamp protocols

All voltage protocols are shown in the relevant figure legends and have been described in detail elsewhere (8, 19, 71).

Isochronal voltage dependence of activation (closed-to-open transition) was measured using a voltage-clamp protocol in which cells were depolarized, from a holding potential of −90 mV to membrane potentials in the range of −60 to +50 mV (test potential), in 10-mV increments, for 1 s to fully open and then inactivate Kv11.1 channels. The membrane potential was then repolarized to −70 mV (or −60 mV for LQTS2-associated mutant channels) for 500 ms, to allow channels to recover from inactivation and transition back into the open state. Peak tail currents measured during this step were normalized to the maximum tail current value (I_{max}) and plotted against the test potential. The resulting isochronal activation curves represent the voltage dependence of the steady-state distribution between the groups of closed and open states, which we analyzed using a simple Boltzmann function (Equation 1),

$$\frac{I}{I_{max}} = \left[\frac{1 + \exp(V_{0.5} - V_t)}{k}\right]^{-1} \quad \text{(Eq. 1)}$$

where I/I_{max} is the current normalized to the maximum; $V_{0.5}$ is the half-maximal activation voltage; V_t is the test potential, and k is the slope. The same data were also fitted with the thermodynamic form of the Boltzmann expression (Equation 2),

$$\frac{g}{g_{max}} = \left[\frac{1 + \exp(\Delta G_0 - z_g EF)}{RT}\right]^{-1} \quad \text{(Eq. 2)}$$

where ΔG_0 is the difference in Gibb's free energy between the states at 0 mV; z_g is the effective number of electric charges crossing the transmembrane electric field; F is Faradays constant; R is the universal gas constant; and T is absolute temperature. Values of $V_{0.5}$, k, and ΔG, for WT and all mutant channels, are given in supplemental Table 1, along with the number of replicates. Perturbations to the Gibb's free energy difference between the closed and open states, for mutants (Mt) compared with WT, were calculated as shown in Equation 3,

$$\Delta\Delta G = \Delta G_{Mt\ or\ WT} - \Delta G_{WT}{}^{mean} \quad \text{(Eq. 3)}$$

where $\Delta G_{Mt\ or\ WT}$ was from individual experiments and $\Delta G_{WT}{}^{mean}$ was the mean ΔG value from all WT replicates.

The rate of activation was measured using an envelope of tails protocol (8). From a holding potential of −90 mV, cells were depolarized to a test potential of +20 mV for increasing times, starting at 10 ms and ending at 3 s. Cells were then repolarized to the tail potential of −70 mV to measure the peak tail current. The longer the time step at the test potential, the more channels have chance to open, and hence the larger the peak tail current up to the point where the maximal number of available channels were open. Peak tail currents were plotted against the increasing time steps, and the data were fitted with a single exponential function to obtain a single time constant for activation ($\tau_{act,\ +20\ mV}$), which are given in supplemental Table 1. For LQTS2-associated mutants, the protocol was performed at a test potential of +40 mV, and a tail potential of −60 mV, to generate $\tau_{act,\ +40\ mV}$, which was compared with equivalent WT data. For all mutants, perturbations, relative to WT, were calculated using Equation 4,

$$\Delta \ln k_{activation,\ \times\ mV} = \Delta \ln k_{Mt} - \Delta \ln k_{WT} \quad \text{(Eq. 4)}$$

where $\ln k_{activation,\ \times\ mV}$ is the natural logarithm of the rate of activation, calculated from $\tau_{act,\ \times\ mV}$. A $-\Delta \ln k_{activation,\ +20\ mV}$ shift greater than ± 0.693 s^{-1} represents a doubling or halving of the rate and is considered biologically significant.

The rate of deactivation (open-to-closed transition) was measured using a double-step protocol. From a holding potential of

−90 mV, cells were depolarized to +40 mV (or +80 mV for some mutants) for 1 s, to open and then inactivate channels. Cells were then repolarized to a range of tail potentials between −50 to −150 mV in 10-mV increments. The decaying portion of the tail currents was then fitted with a double-exponential function to obtain the fast ($\tau_{\text{fast, }X\text{ mV}}$) and slow ($\tau_{\text{slow, }X\text{ mV}}$) time constants for deactivation at each tail potential. For each mutant (mut) and WT, we used a weighted time constant for deactivation measured as shown in Equation 5,

$$\tau_{\text{mut or WT}} = \frac{(\lambda_{\tau\text{fast}} \cdot \tau_{\text{fast}} + \lambda_{\tau\text{slow}} \cdot \tau_{\text{slow}})}{\lambda_{\tau\text{fast}} + \lambda_{\tau\text{slow}}} \quad \text{(Eq. 5)}$$

where τ_{fast} and τ_{slow} are the fast and slow time constants, respectively, and $\lambda_{\tau\text{fast}}$ and $\lambda_{\tau\text{slow}}$ are the relative proportions of the fast and slow components, respectively (shown for WT and all mutants in supplemental Table 2, along with the number of replicates). Perturbations to the rate of deactivation were calculated as $-\Delta\ln k_{\text{deactivation, }X\text{ mV}}$, using a modified version of Equation 4.

Rates for the onset of inactivation (open-to-inactivated transition) were measured using a triple-pulse protocol (8). From a holding potential of −90 mV, cells were depolarized to +40 mV (or +80 mV for some mutants) for 1 s to activate and then inactivate Kv11.1 channels. Voltage was then stepped to −110 mV for 10 ms to allow recovery from inactivation. A third step to voltages in the range of +60 mV to −60 mV, in 10-mV increments, was then used to monitor the onset of inactivation. A single-exponential function was fitted to the decaying portion of the current to attain the forward rate (k_{onset}) at each voltage (V). The reverse rates (k_{rec}), which represent the recovery from inactivation (inactivated-to-open transition), were measured from the same two-step voltage protocol used to measure the rate of deactivation (see above). At each tail voltage, Kv11.1 currents show an initial fast rising tail current, before deactivating, which is due to channels recovering from the inactivated state into the open state. This produces a characteristic "hooked" tail current (8) which was then fitted with a double-exponential function (to ensure an accurate fit), where the fast time constant reflects the rate of recovery from inactivation. The observed rates for inactivation ($k_{\text{obs, V}} = k_{\text{onset, V}} + k_{\text{rec, V}}$) at each voltage were then plotted to generate a chevron plot, as shown previously and in Fig. 6 (71). The two linear arms of the chevron plot, at the two extremes of voltage, represent the unidirectional rate constants for the onset of inactivation and recovery from inactivation. Unidirectional rate constants were then extrapolated to obtain values for k_{onset} ($k_{\text{onset, 0 mV}}$) and k_{recovery} ($k_{\text{recovery, 0 mV}}$) at 0 mV. The equilibrium constant ($K_{\text{eq, 0 mV}}$) for inactivation represents the voltage dependence of inactivation and can be calculated using Equation 6,

$$K_{\text{eq(0, mV)}} = \frac{k_{\text{Onset, 0 mV}}}{k_{\text{recovery, 0 mV}}} \quad \text{(Eq. 6)}$$

For each WT or mutant channel, values of $k_{\text{onset, 0 mV}}$, $k_{\text{recovery, 0 mV}}$, and $K_{\text{eq, 0 mV}}$ are given in supplemental Table 3, along with the number of replicates. Perturbations to the rate of onset of inactivation ($\Delta\ln k_{\text{onset, 0 mV}}$) or recovery from inactivation ($\Delta\ln k_{\text{recovery, 0 mV}}$) were calculated using a modified version of Equation 4. Gibb's free energy differences for the equilibrium for inactivation ($\Delta G_{\text{Eq, 0 mV}}$), were calculated from the K_{eq} values using Equation 7, and $\Delta\Delta G$ values were calculated according to Equation 3.

$$\Delta G_{\text{eq, }\times\text{ mV}} = -\text{RT} \cdot \ln K_{\text{eq, }\times\text{ mV}} \quad \text{(Eq. 7)}$$

The degree to which LQTS2-associated mutations in the pre-S1 or S1 region perturb the amount of current contributing to cardiac repolarization was assessed using a step-ramp voltage-clamp protocol designed to mimic a ventricular action potential (shown in Fig. 9). From a holding potential of −80 mV, cells were depolarized to +30 mV (the step) for 500 ms, to mimic the plateau phase of the action potential, before a ramp repolarization back to −80 mV over 220 ms, to mimic the repolarizing phase of the action potential. To correct for capacitance artifacts during the ramp repolarization phase, the instantaneous drop in current observed at the onset of the ramp repolarization phase was subtracted from the repolarizing current. Variable expression levels observed between cells were compensated for by normalizing current to the whole-cell conductance, measured in the same cell from the peak negative currents elicited at voltages between −140 to −160 mV following a 1-s depolarization at +40 mV, as described previously (19). In addition to the effect on the repolarizing current, we also wished to examine the extent to which LQTS2-associated mutants in the pre-S1 or S1 region alter the amount of protective current elicited in response to premature beats. For this, we delivered premature depolarizations (to 0 mV for 40 ms) at 20-ms intervals, starting 120 ms after the onset of the ramp repolarization phase of the step-ramp protocol (see Fig. 9*E*) (19). At each time point, the peak protective current was measured by fitting with a single exponential function and extrapolating back to the start of the 0-mV voltage step. This fitting process was necessary to eliminate capacitance spike artifacts. Peak currents were also normalized to the whole-cell conductance to compensate for variable expression levels.

Western blotting analysis of protein expression

For Western blotting studies, the Kv11.1 cDNA was subcloned into pIRES2-eGFP, a bicistronic mammalian expression vector that co-expresses GFP. HA-tagged WT or mutant Kv11.1 constructs were transfected into HEK293 cells using the Lipofectamine 2000 transfection reagent (Life Technologies, Inc., Mulgrave, Victoria Australia) with 200 ng of DNA. Cells were maintained in Dulbecco's modified Eagle's medium (DMEM, Life Technologies, Inc.) supplemented with 10% fetal bovine serum (Life Technologies, Inc.) and stored at 37 °C with 5% CO_2. Cells were harvested 48 h after transfection and then solubilized in Tris-buffered saline (TBS, in mM: 50 Tris, 137 NaCl, pH 7.5) supplemented with 1% Nonidet P-40 and a protease inhibitor mixture (Roche Diagnostics, Castle Hill, New South Wales, Australia) for 1 h on a rotating wheel at 4 °C. Cell lysates were cleared by centrifugation at 16,000 × *g* at 4 °C for 30 min. Lysates were then mixed with SDS-PAGE sample buffer containing 5% β-mercaptoethanol and then loaded and run on a 7.5% SDS-polyacrylamide gel before transfer to nitrocellulose membrane (Bio-Rad, Gladesville, New South Wales, Australia).

For quantitative Western blotting analysis, membranes were probed simultaneously with mouse monoclonal anti-HA antibody (HA.11, Covance, Princeton, NJ) and a rabbit or mouse anti-α-actinin antibody (Santa Cruz Biotechnology), followed by anti-rabbit IRDye680 or anti-mouse IRDye800 to enable quantification with the Li-Cor Odyssey infrared imaging system (Li-Cor Biotechnology, Lincoln, NE).

Kv11.1 channel protein was represented by two bands on the Western blot: a fully glycosylated band (FG, ~155 kDa), which predominantly represents channel protein at the cell membrane where it is functional, and a core-glycosylated band (CG, ~135 kDa), which represents immature protein that is intracellular and thus non-functional. To account for changes in expression levels arising from different transfection efficiencies, the density of the FG band was normalized to the GFP level measured from the same cells. For each experiment, the mutant FG/GFP ratio was compared with corresponding measures from a WT construct expressed on the same day (*i.e.* mutants were normalized to WT). Because FG/GFP values were always normalized to WT protein (including for WT itself), the WT was expressed as 1 in every experiment, and so no error bars are shown for WT (WT data from $n = 17$ experiments). An FG/GFP value of 0 indicates the absence of membrane Kv11.1 protein on Western blots, 1 indicates an expression level comparable with WT (no defect) and >1 indicates improved expression compared with WT.

Author contributions—K. P. conducted electrophysiology experiments and drafted the paper. C. A. N. analyzed the NMR data, conducted the experiments, and contributed to writing the paper. E. D. conducted electrophysiology experiments. D. S. conducted the NMR experiments and analyzed the data. P. W. K. conducted NMR experiments and critically reviewed the paper. J. I. V. helped conceive the idea for the project, interpreted the data, and critically reviewed the paper. M. D. P. conceived the idea for the project, performed the experiments, analyzed and interpreted the data, and wrote the paper.

Acknowledgments—We thank T. Marciniec and M. J. Hunter for help making some of the mutants used in this study.

References

1. Sanguinetti, M. C., Jiang, C., Curran, M. E., and Keating, M. T. (1995) A mechanistic link between an inherited and an acquired cardiac arrhythmia: HERG encodes the IKr potassium channel. *Cell* **81,** 299–307
2. Lu, Y., Mahaut-Smith, M. P., Varghese, A., Huang, C. L., Kemp, P. R., and Vandenberg, J. I. (2001) Effects of premature stimulation on HERG K^+ channels. *J. Physiol.* **537,** 843–851
3. Smith, P. L., Baukrowitz, T., and Yellen, G. (1996) The inward rectification mechanism of the HERG cardiac potassium channel. *Nature* **379,** 833–836
4. Curran, M. E., Splawski, I., Timothy, K. W., Vincent, G. M., Green, E. D., and Keating, M. T. (1995) A molecular basis for cardiac arrhythmia: HERG mutations cause long QT syndrome. *Cell* **80,** 795–803
5. Moss, A. J., Zareba, W., Kaufman, E. S., Gartman, E., Peterson, D. R., Benhorin, J., Towbin, J. A., Keating, M. T., Priori, S. G., Schwartz, P. J., Vincent, G. M., Robinson, J. L., Andrews, M. L., Feng, C., Hall, W. J., *et al.* (2002) Increased risk of arrhythmic events in long-QT syndrome with mutations in the pore region of the human ether-a-go-go-related gene potassium channel. *Circulation* **105,** 794–799
6. Shimizu, W., Moss, A. J., Wilde, A. A., Towbin, J. A., Ackerman, M. J., January, C. T., Tester, D. J., Zareba, W., Robinson, J. L., Qi, M., Vincent, G. M., Kaufman, E. S., Hofman, N., Noda, T., Kamakura, S., *et al.* (2009) Genotype-phenotype aspects of type 2 long QT syndrome. *J. Am. Coll. Cardiol.* **54,** 2052–2062
7. Splawski, I., Shen, J., Timothy, K. W., Lehmann, M. H., Priori, S., Robinson, J. L., Moss, A. J., Schwartz, P. J., Towbin, J. A., Vincent, G. M., and Keating, M. T. (2000) Spectrum of mutations in long-QT syndrome genes. KVLQT1, HERG, SCN5A, KCNE1, and KCNE2. *Circulation* **102,** 1178–1185
8. Vandenberg, J. I., Perry, M. D., Perrin, M. J., Mann, S. A., Ke, Y., and Hill, A. P. (2012) hERG K^+ channels: structure, function, and clinical significance. *Physiol. Rev.* **92,** 1393–1478
9. Zhang, T., Moss, A., Cong, P., Pan, M., Chang, B., Zheng, L., Fang, Q., Zareba, W., Robinson, J., Lin, C., Li, Z., Wei, J., Zeng, Q., Long, Q. T., International Registry Investigators, HVP-China Investigators, and Qi, M. (2010) LQTS gene LOVD database. *Hum. Mutat.* **31,** E1801–E1810
10. Gong, Q., Zhang, L., Vincent, G. M., Horne, B. D., and Zhou, Z. (2007) Nonsense mutations in hERG cause a decrease in mutant mRNA transcripts by nonsense-mediated mRNA decay in human long-QT syndrome. *Circulation* **116,** 17–24
11. Anderson, C. L., Delisle, B. P., Anson, B. D., Kilby, J. A., Will, M. L., Tester, D. J., Gong, Q., Zhou, Z., Ackerman, M. J., and January, C. T. (2006) Most LQT2 mutations reduce Kv11.1 (hERG) current by a class 2 (trafficking-deficient) mechanism. *Circulation* **113,** 365–373
12. Anderson, C. L., Kuzmicki, C. E., Childs, R. R., Hintz, C. J., Delisle, B. P., and January, C. T. (2014) Large-scale mutational analysis of Kv11.1 reveals molecular insights into type 2 long QT syndrome. *Nat. Commun.* **5,** 5535
13. Gong, Q., Keeney, D. R., Molinari, M., and Zhou, Z. (2005) Degradation of trafficking-defective long QT syndrome type II mutant channels by the ubiquitin-proteasome pathway. *J. Biol. Chem.* **280,** 19419–19425
14. Ke, Y., Ng, C. A., Hunter, M. J., Mann, S. A., Heide, J., Hill, A. P., and Vandenberg, J. I. (2013) Trafficking defects in PAS domain mutant Kv11.1 channels: roles of reduced domain stability and altered domain-domain interactions. *Biochem. J.* **454,** 69–77
15. Zhao, J. T., Hill, A. P., Varghese, A., Cooper, A. A., Swan, H., Laitinen-Forsblom, P. J., Rees, M. I., Skinner, J. R., Campbell, T. J., and Vandenberg, J. I. (2009) Not all hERG pore domain mutations have a severe phenotype: G584S has an inactivation gating defect with mild phenotype compared to G572S, which has a dominant negative trafficking defect and a severe phenotype. *J. Cardiovasc. Electrophysiol.* **20,** 923–930
16. Balijepalli, S. Y., Lim, E., Concannon, S. P., Chew, C. L., Holzem, K. E., Tester, D. J., Ackerman, M. J., Delisle, B. P., Balijepalli, R. C., and January, C. T. (2012) Mechanism of loss of Kv11.1 K+ current in mutant T421M-Kv11.1-expressing rat ventricular myocytes: interaction of trafficking and gating. *Circulation* **126,** 2809–2818
17. Berecki, G., Zegers, J. G., Verkerk, A. O., Bhuiyan, Z. A., de Jonge, B., Veldkamp, M. W., Wilders, R., and van Ginneken, A. C. (2005) HERG channel (dys)function revealed by dynamic action potential clamp technique. *Biophys. J.* **88,** 566–578
18. Kanters, J. K., Skibsbye, L., Hedley, P. L., Dembic, M., Liang, B., Hagen, C. M., Eschen, O., Grunnet, M., Christiansen, M., and Jespersen, T. (2015) Combined gating and trafficking defect in Kv11.1 manifests as a malignant long QT syndrome phenotype in a large Danish p.F29L founder family. *Scand. J. Clin. Lab. Invest.* **75,** 699–709
19. Perry, M. D., Ng, C. A., Phan, K., David, E., Steer, K., Hunter, M. J., Mann, S. A., Imtiaz, M., Hill, A. P., Ke, Y., and Vandenberg, J. I. (2016) Rescue of protein expression defects may not be enough to abolish the pro-arrhythmic phenotype of long QT type 2 mutations. *J. Physiol.* **594,** 4031–4049
20. Gustina, A. S., and Trudeau, M. C. (2009) A recombinant N-terminal domain fully restores deactivation gating in N-truncated and long QT syndrome mutant hERG potassium channels. *Proc. Natl. Acad. Sci. U.S.A.* **106,** 13082–13087
21. Morais Cabral, J. H., Lee, A., Cohen, S. L., Chait, B. T., Li, M., and Mackinnon, R. (1998) Crystal structure and functional analysis of the HERG potassium channel N terminus: a eukaryotic PAS domain. *Cell* **95,** 649–655

22. Ng, C. A., Phan, K., Hill, A. P., Vandenberg, J. I., and Perry, M. D. (2014) Multiple interactions between cytoplasmic domains regulate slow deactivation of Kv11.1 channels. *J. Biol. Chem.* **289,** 25822–25832
23. Wang, J., Myers, C. D., and Robertson, G. A. (2000) Dynamic control of deactivation gating by a soluble amino-terminal domain in HERG K(+) channels. *J. Gen. Physiol.* **115,** 749–758
24. Spector, P. S., Curran, M. E., Zou, A., Keating, M. T., and Sanguinetti, M. C. (1996) Fast inactivation causes rectification of the IKr channel. *J. Gen. Physiol.* **107,** 611–619
25. Long, S. B., Campbell, E. B., and Mackinnon, R. (2005) Voltage sensor of Kv1.2: structural basis of electromechanical coupling. *Science* **309,** 903–908
26. Tristani-Firouzi, M., Chen, J., and Sanguinetti, M. C. (2002) Interactions between S4-S5 linker and S6 transmembrane domain modulate gating of HERG K^+ channels. *J. Biol. Chem.* **277,** 18994–19000
27. Tan, P. S., Perry, M. D., Ng, C. A., Vandenberg JI, and Hill, A. P. (2012) Voltage-sensing domain mode shift is coupled to the activation gate by the N-terminal tail of hERG channels. *J. Gen. Physiol.* **140,** 293–306
28. Liu, J., Zhang, M., Jiang, M., and Tseng, G. N. (2003) Negative charges in the transmembrane domains of the HERG K channel are involved in the activation- and deactivation-gating processes. *J. Gen. Physiol.* **121,** 599–614
29. Zhang, M., Liu, J., Jiang, M., Wu, D. M., Sonawane, K., Guy, H. R., and Tseng, G. N. (2005) Interactions between charged residues in the transmembrane segments of the voltage-sensing domain in the hERG channel. *J. Membr. Biol.* **207,** 169–181
30. Papazian, D. M., Shao, X. M., Seoh, S. A., Mock, A. F., Huang, Y., and Wainstock, D. H. (1995) Electrostatic interactions of S4 voltage sensor in Shaker K+ channel. *Neuron* **14,** 1293–1301
31. Piper, D. R., Rupp, J., Sachse, F. B., Sanguinetti, M. C., and Tristani-Firouzi, M. (2008) Cooperative interactions between R531 and acidic residues in the voltage sensing module of hERG1 channels. *Cell. Physiol. Biochem.* **21,** 37–46
32. Lacroix, J. J., Pless, S. A., Maragliano, L., Campos, F. V., Galpin, J. D., Ahern, C. A., Roux, B., and Bezanilla, F. (2012) Intermediate state trapping of a voltage sensor. *J. Gen. Physiol.* **140,** 635–652
33. Haitin, Y., Yisharel, I., Malka, E., Shamgar, L., Schottelndreier, H., Peretz, A., Paas, Y., and Attali, B. (2008) S1 constrains S4 in the voltage sensor domain of Kv7.1 K+ channels. *PLoS One* **3,** e1935
34. Bocksteins, E., Ottschytsch, N., Timmermans, J. P., Labro, A. J., and Snyders, D. J. (2011) Functional interactions between residues in the S1, S4, and S5 domains of Kv2.1. *Eur. Biophys. J.* **40,** 783–793
35. Colenso, C. K., Sessions, R. B., Zhang, Y. H., Hancox, J. C., and Dempsey, C. E. (2013) Interactions between voltage sensor and pore domains in a hERG K+ channel model from molecular simulations and the effects of a voltage sensor mutation. *J. Chem. Inf. Model.* **53,** 1358–1370
36. Lee, S. Y., Banerjee, A., and MacKinnon, R. (2009) Two separate interfaces between the voltage sensor and pore are required for the function of voltage-dependent K(+) channels. *PLoS Biol.* **7,** e47
37. Long, S. B., Tao, X., Campbell, E. B., and MacKinnon, R. (2007) Atomic structure of a voltage-dependent K+ channel in a lipid membrane-like environment. *Nature* **450,** 376–382
38. Hite, R. K., Yuan, P., Li, Z., Hsuing, Y., Walz, T., and MacKinnon, R. (2015) Cryo-electron microscopy structure of the Slo2.2 Na(+)-activated K(+) channel. *Nature* **527,** 198–203
39. Hite, R. K., Tao, X., and MacKinnon, R. (2017) Structural basis for gating the high-conductance Ca2+-activated K+ channel. *Nature* **541,** 52–57
40. Tao, X., Hite, R. K., and MacKinnon, R. (2017) Cryo-EM structure of the open high-conductance Ca2+-activated K+ channel. *Nature* **541,** 46–51
41. Liao, M., Cao, E., Julius, D., and Cheng, Y. (2013) Structure of the TRPV1 ion channel determined by electron cryo-microscopy. *Nature* **504,** 107–112
42. Saotome, K., Singh, A. K., Yelshanskaya, M. V., and Sobolevsky, A. I. (2016) Crystal structure of the epithelial calcium channel TRPV6. *Nature* **534,** 506–511
43. Zubcevic, L., Herzik, M. A., Jr., Chung, B. C., Liu, Z., Lander, G. C., and Lee, S. Y. (2016) Cryo-electron microscopy structure of the TRPV2 ion channel. *Nat. Struct. Mol. Biol.* **23,** 180–186
44. Paulsen, C. E., Armache, J. P., Gao, Y., Cheng, Y., and Julius, D. (2015) Structure of the TRPA1 ion channel suggests regulatory mechanisms. *Nature* **520,** 511–517
45. Garcia-Elias, A., Berna-Erro, A., Rubio-Moscardo, F., Pardo-Pastor, C., Mrkonjić, S., Sepúlveda, R. V., Vicente, R., González-Nilo, F., and Valverde, M. A. (2015) Interaction between the linker, pre-S1, and TRP domains determines folding, assembly, and trafficking of TRPV channels. *Structure* **23,** 1404–1413
46. Cheng, Y. M., and Claydon, T. W. (2012) Voltage-dependent gating of HERG potassium channels. *Front. Pharmacol.* **3,** 83
47. Dhillon, M. S., Cockcroft, C. J., Munsey, T., Smith, K. J., Powell, A. J., Carter, P., Wrighton, D. C., Rong, H. L., Yusaf, S. P., and Sivaprasadarao, A. (2014) A functional Kv1.2-hERG chimaeric channel expressed in *Pichia pastoris*. *Sci. Rep.* **4,** 4201
48. Es-Salah-Lamoureux, Z., Fougere, R., Xiong, P. Y., Robertson, G. A., and Fedida, D. (2010) Fluorescence-tracking of activation gating in human ERG channels reveals rapid S4 movement and slow pore opening. *PLoS ONE* **5,** e10876
49. Zhang, M., Liu, J., and Tseng, G. N. (2004) Gating charges in the activation and inactivation processes of the HERG channel. *J. Gen. Physiol.* **124,** 703–718
50. Whicher, J. R., and MacKinnon, R. (2016) Structure of the voltage-gated K(+) channel Eag1 reveals an alternative voltage sensing mechanism. *Science* **353,** 664–669
51. Pintacuda, G., and Otting, G. (2002) Identification of protein surfaces by NMR measurements with a paramagnetic Gd(III) chelate. *J. Am. Chem. Soc.* **124,** 372–373
52. Hong, K. H., and Miller, C. (2000) The lipid-protein interface of a Shaker K(+) channel. *J. Gen. Physiol.* **115,** 51–58
53. Koval, O. M., Fan, Y., and Rothberg, B. S. (2007) A role for the S0 transmembrane segment in voltage-dependent gating of BK channels. *J. Gen. Physiol.* **129,** 209–220
54. Li-Smerin, Y., Hackos, D. H., and Swartz, K. J. (2000) A localized interaction surface for voltage-sensing domains on the pore domain of a K+ channel. *Neuron* **25,** 411–423
55. Monks, S. A., Needleman, D. J., and Miller, C. (1999) Helical structure and packing orientation of the S2 segment in the Shaker K+ channel. *J. Gen. Physiol.* **113,** 415–423
56. Subbiah, R. N., Kondo, M., Campbell, T. J., and Vandenberg, J. I. (2005) Tryptophan scanning mutagenesis of the HERG K+ channel: the S4 domain is loosely packed and likely to be lipid exposed. *J. Physiol.* **569,** 367–379
57. Lanigan, M. D., Kalman, K., Lefievre, Y., Pennington, M. W., Chandy, K. G., and Norton, R. S. (2002) Mutating a critical lysine in ShK toxin alters its binding configuration in the pore-vestibule region of the voltage-gated potassium channel, Kv1.3. *Biochemistry* **41,** 11963–11971
58. Wang, D. T., Hill, A. P., Mann, S. A., Tan, P. S., and Vandenberg, J. I. (2011) Mapping the sequence of conformational changes underlying selectivity filter gating in the K(v)11.1 potassium channel. *Nat. Struct. Mol. Biol.* **18,** 35–41
59. von Heijne, G. (1991) Proline kinks in transmembrane α-helices. *J. Mol. Biol.* **218,** 499–503
60. Gianulis, E. C., Liu, Q., and Trudeau, M. C. (2013) Direct interaction of eag domains and cyclic nucleotide-binding homology domains regulate deactivation gating in hERG channels. *J. Gen. Physiol.* **142,** 351–366
61. de la Peña, P., Alonso-Ron, C., Machín, A., Fernández-Trillo, J., Carretero, L., Domínguez, P., and Barros, F. (2011) Demonstration of physical proximity between the N terminus and the S4-S5 linker of the human ether-a-go-go-related gene (hERG) potassium channel. *J. Biol. Chem.* **286,** 19065–19075
62. Vandenberg, J. I., Varghese, A., Lu, Y., Bursill, J. A., Mahaut-Smith, M. P., and Huang, C. L. (2006) Temperature dependence of human ether-a-go-go-related gene K+ currents. *Am. J. Physiol. Cell Physiol.* **291,** C165–C175
63. Gianulis, E. C., and Trudeau, M. C. (2011) Rescue of aberrant gating by a genetically encoded PAS (Per-Arnt-Sim) domain in several long QT syn-

drome mutant human ether-a-go-go-related gene potassium channels. *J. Biol. Chem.* **286,** 22160–22169
64. Chen, J., Zou, A., Splawski, I., Keating, M. T., and Sanguinetti, M. C. (1999) Long QT syndrome-associated mutations in the Per-Arnt-Sim (PAS) domain of HERG potassium channels accelerate channel deactivation. *J. Biol. Chem.* **274,** 10113–10118
65. Liu, Q. N., and Trudeau, M. C.. (2015) Eag domains regulate LQT mutant hERG channels in human induced pluripotent stem cell-derived cardiomyocytes. *PLoS ONE* **10,** e0123951
66. Bax, A., and Davis, D. G. (1985) Mlev-17-based two-dimensional homonuclear magnetization transfer spectroscopy. *J. Magn. Reson.* 65, 355–360
67. Kumar, A., Ernst, R. R., and Wüthrich, K. (1980) A two-dimensional nuclear Overhauser enhancement (2D NOE) experiment for the elucidation of complete proton-proton cross-relaxation networks in biological macromolecules. *Biochem. Biophys. Res. Commun.* **95,** 1–6
68. Guex, N., and Peitsch, M. C. (1997) SWISS-MODEL and the Swiss-PdbViewer: an environment for comparative protein modeling. *Electrophoresis* **18,** 2714–2723
69. Arnold, K., Bordoli, L., Kopp, J., and Schwede, T. (2006) The SWISS-MODEL workspace: a web-based environment for protein structure homology modelling. *Bioinformatics* **22,** 195–201
70. Bordoli, L., Kiefer, F., Arnold, K., Benkert, P., Battey, J., and Schwede, T. (2009) Protein structure homology modeling using SWISS-MODEL workspace. *Nat. Protoc.* **4,** 1–13
71. Perry, M. D., Ng, C. A., and Vandenberg, J. I. (2013) Pore helices play a dynamic role as integrators of domain motion during Kv11.1 channel inactivation gating. *J. Biol. Chem.* **288,** 11482–11491